Optical Materials 163 (2025) 116965

Contents lists available at ScienceDirect

Optical Materials

journal homepage: www.elsevier.com/locate/optmat

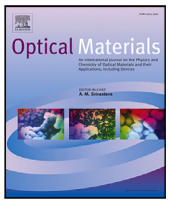

Research Article

Optical spectroscopy of exchange-coupled ions: Insights into homonuclear, heteronuclear and mixed transition-metal/rare-earth systems

Diego Pérez-Francés [a], Fernando Rodríguez [b], Rafael Valiente [a,*]

[a] Departamento de Física Aplicada, Universidad de Cantabria, Avenida de los Castros, Santander, 39005, Cantabria, Spain
[b] Departamento CITIMAC, Universidad de Cantabria, Avenida de los Castros, Santander, 39005, Cantabria, Spain

ARTICLE INFO

Keywords:
Optical spectroscopy
Exchange interaction
Superexchange
Exchange-coupled systems
High pressure

ABSTRACT

In 1988, McCarthy and Güdel published the seminal review *Optical Spectroscopy of Exchange-Coupled Transition Metal Complexes*, which not only compiled key spectroscopic results but also provided a deep insight into the theoretical foundations of the field, originally developed by Tanabe in the 1960s, which is undoubtedly the most insightful review in this topic to date. The work presented here aims to pay a modest tribute to Prof. Hans U. Güdel for his outstanding contributions and career — a scientist who was a guiding figure for many of us entering the field of spectroscopy. This review provides an updated overview of key experimental findings where exchange-coupled systems play a fundamental role, many of which involved direct contributions from Prof. Güdel himself. We begin by discussing homonuclear transition-metal systems, such as Mn^{2+}–Mn^{2+} and Mn^{3+}–Mn^{3+} pairs, highlighting the unique features of their absorption and emission spectra, as well as their lifetimes — phenomena that are not observed in isolated ions. The discussion then extends to heteronuclear mixed-metal systems, specifically transition-metal/rare-earth ion pairs, such as Mn^{2+}–Yb^{3+}. In these systems, a novel upconversion luminescence mechanism was proposed, based on exchange interaction via the Tanabe mechanism between Yb^{3+} and Mn^{2+}. Significant enhancement of optical absorption and its temperature dependence was attributed to Mn^{2+}–Cu^{2+} exchange interaction units. Finally, we compare results from two Ni^{2+}-doped isostructural materials — Rb_2CdCl_4 and Rb_2MnCl_4 — emphasizing the potential of exchange coupling mechanism to enhance luminescence efficiency.

1. Introduction

Hans U. Güdel, an outstanding spectroscopist, has made significant contributions to the understanding and development of exchange-coupled systems. His work provided profound insights into the magnetic and electronic properties of transition metal and rare earth complexes. This article aims to honor Prof. Güdel's legacy by expanding his review, mainly focusing on his work with exchange-coupled systems and their influence on spectroscopic measurements.

Exchange interactions, fundamental to the field of magnetism and spectroscopy, arise from the quantum mechanical principles governing the interaction between orbitals and spins of electrons. In a exchange-coupled system, unpaired electrons in distinct paramagnetic centers interact, leading to different configurations of magnetic moments. This interaction is a result of the Pauli exclusion principle and Coulomb repulsion, both determining the energy states of the system.

The spectroscopy of exchange-coupled systems has been a topic of interest since the pioneering works of Schawlow [1], McClure [2], Tanabe [3], and Ferguson [4]. In 1988, McCarthy and Güdel [5] conducted the first review on the advances in the spectroscopy of exchange-coupled transition metal ions.

When two or more paramagnetic centers with an incomplete *d*-orbital occupancy are close enough to experience a significant exchange interaction, the resulting coordination complex can behave as a new optical center, acquiring unique spectroscopic properties that differ from those of the individual centers [6]. Exchange interactions are classified based on their nature and strength:

- Direct exchange: This occurs when there is a direct overlap between the wavefunctions of unpaired electrons in adjacent atoms or ions. This type of exchange is typically observed in systems with close-packed structures and dimeric species of close faced ions.
- Indirect exchange (superexchange): When the magnetic centers are not directly bonded but interact through a non-magnetic anion.

* Corresponding author.
E-mail address: rafael.valiente@unican.es (R. Valiente).

https://doi.org/10.1016/j.optmat.2025.116965
Received 1 February 2025; Received in revised form 17 March 2025; Accepted 19 March 2025
Available online 28 March 2025

- Double exchange: Relevant in mixed-valence compounds, double exchange involves the transfer of an electron between ions of different oxidation states, mediated by a bridging ligand. This mechanism is essential in explaining the magnetism in materials like manganites.
- Anisotropic exchange (Dzyaloshinskii–Moriya interaction): This type of interaction arises in systems lacking inversion symmetry and involves spin–orbit coupling.

This review focuses on the optical spectroscopy (absorption and luminescence) of exchange-coupled homonuclear pairs of Mn^{2+} and Mn^{3+}, as well as heteronuclear systems of Mn^{2+} with other transition metal ions (Ni^{2+} or Cu^{2+}) and rare-earth ions (Yb^{3+}).

Exchange interactions have been observed in both $3d^n$ transition metal ion pairs and $4f^n$ ion pairs. However, because the $4f^n$ electrons of lanthanides are shielded from surrounding ions by $5s$ and $5p$ electrons, this interaction is significantly weaker in the case of lanthanide ion pairs [7]. Depending on the atomic orbitals involved and the symmetry of the system, the exchange coupling can be ferromagnetic or antiferromagnetic in nature.

The spectra of dimers where the two ions are coupled via exchange interactions provide a tool for investigating fundamental magnetic interactions at a basic level, focusing on just two coupled ions rather than the collective behavior of the entire material [6]. Since this phenomenon is related to the pairing of electron spins, common experimental methods include magnetic susceptibility measurements, electron spin resonance spectroscopy, and inelastic neutron scattering [5]. While optical techniques such as emission and absorption spectroscopy are often considered complementary, in many cases they can provide information that cannot be obtained using the aforementioned methods. Furthermore, optical spectroscopy, at variance with commonly used methods, provides information on the exchange interactions related, not only to the ground state but also to excited states. This characteristic makes it unique for exploring magnetism of excited states.

The first observation of the effects of exchange-coupled ions in optical spectroscopy was performed by Schawlow et al. [1] in ruby with high Cr^{3+} concentrations. The appearance of new absorption and emission lines, which were absent in samples with lower concentrations, was attributed to the formation of Cr^{3+} pairs (Fig. 1). The two emissions in the 6900–6940 Å range correspond to the well-known R_1 and R_2 lines of ruby ($^2E \rightarrow {}^4A_2$ transition). As the ion concentration increases, new emission lines appear, revealing an additional fine structure at larger wavelengths in the emission spectrum. Interestingly, these new emissions (associated with Cr^{3+} pairs formed due to the increased concentration) grow in intensity while the intensity of the single-ion R_1 and R_2 lines decreases.

Following this discovery, other systems were investigated [8–12] including both pure and doped materials. These studies encompassed homonuclear pairs (e.g., Cr^{3+} [11] or Mn^{2+} [10]) and heteronuclear pairs (e.g., Mn^{2+}-Ni^{2+} [9]), with the latter exhibiting more pronounced exchange-coupling effects. Shortly thereafter, the first studies on mixed systems emerged, involving lanthanide and transition metal ions. Van Der Ziel and Van Uitert [13] provided the first experimental spectroscopic evidence of exchange coupling between Cr^{3+} and Eu^{3+} in $EuAlO_3$:Cr^{3+}.

Vial and Buisson [14] were the first to observe exchange interaction between lanthanide ions, specifically between Pr^{3+} pairs in LaF_3:Pr^{3+}. In this case, the transitions in exchange-coupled dimers are very similar to those of single ions, as the exchange interactions between rare earth ions are much weaker than those between transition metal ions [6]. These findings prompted theoretical interest [3,4,15] aimed at understanding the effects of magnetic (exchange) interactions between paramagnetic ions on spectroscopic properties.

The main phenomena observed in optical spectroscopy associated with the effects of exchange coupling between transition metal ions can be classify depending on whether the d-d transitions are spin-allowed or spin-forbidden [5]:

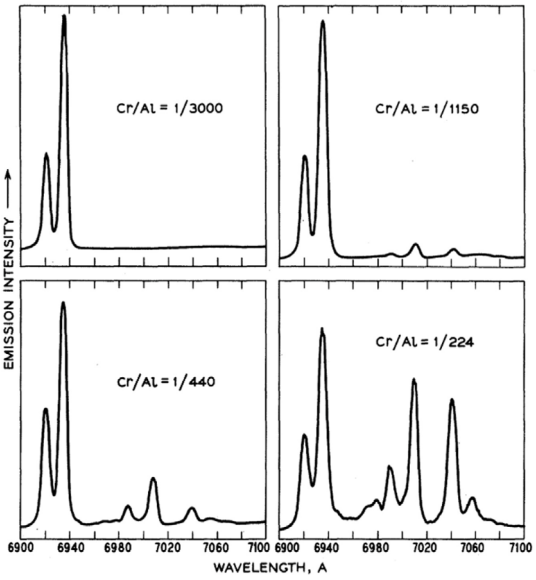

Fig. 1. Luminescence spectrum of ruby at 77 K as a function of Cr^{3+} concentration. This represents the first experimental evidence of optical spectroscopy of exchange-coupled ion pairs. The observed effect is the appearance of an additional fine structure as the Cr^{3+} concentration increases. Reprinted with permission from Schawlow et al. [1]. Copyright (1959) by the American Physical Society.

1. Spin-allowed d-d transitions are practically unaffected by exchange coupling. A clear example is the mixed Mn^{2+}-Ti^{2+} pairs in $MnCl_2$ [16].
2. Spin-forbidden d-d transitions, on the other hand, are significantly influenced by exchange coupling. Although their spectral positions are scarcely affected, they exhibit the following effects:

   a. A remarkable increase in band intensity. For instance, McCarthy and Güdel [17] reported an intensity increase of up to two orders of magnitude for Mn^{2+} transitions in $CsMgBr_3$:Mn^{2+}, attributed to the formation of exchange-coupled dimers. This effect is explained by what was later termed the Tanabe mechanism [3,4,15], which will be discussed later.

   b. The appearance of additional fine structure. As observed in Fig. 1, this is explained by the splitting of the electronic states in the exchange-coupled dimer (see below).

   c. Strong temperature dependence. The presence of *hot bands* is due to the splitting of electronic levels in the ground or excited state (absorption or emission, respectively) caused by exchange coupling effects and the spin selection rules for the dimer. An example, to be discussed in detail, is the *hot bands* observed in $KZnF_3$:Mn^{2+} dimers [4].

   d. New absorption states at energies approximately twice those of single excitations [18], referred to as pair excitations or double excitations.

   e. Additionally, it is important to note that the intensity also shows significant dependence on the polarization of the electric field of the incident light [17,19–21]. When absorption spectra are measured on single crystals, the spectra recorded with $\vec{E} \parallel \vec{c}$ (π) or $\vec{E} \perp \vec{c}$ (σ or α) exhibit differences that can be explained by the Tanabe intensity mechanism [3,4,15] and superexchange pathways.

It is worth adding to this list some effects observed in heteronuclear pairs of transition-metal ions (TM/TM′), such as the exchange enhancement of Ni^{2+} absorption and luminescence in Mn^{2+}–Ni^{2+} dimers [22], or in mixed pairs of transition metal and lanthanide ions (TM/Ln), such as the dependence of upconversion emission efficiency on the superexchange pathway geometry observed in Mn^{2+}–Yb^{3+} dimers [23].

1.1. The splitting of electronic states in exchange-coupled ion pairs

When the electronic charge clouds of two ions overlap, either directly or indirectly through the ligands, the exchange interaction occurs. The interaction in the latter case is known as superexchange, and its magnitude depends on the overlap between the metal and ligand orbitals, and therefore on the bond angle.

Consider two ions with unpaired electrons, labeled A and B. Let $\mathbf{s}_{a_i}$ and $\mathbf{s}_{b_j}$ be the spin operators of the ith electron in the partially occupied orbital a of ion A and the jth electron in the partially occupied orbital b of ion B. The effective interaction Hamiltonian between the spins of both ions can be written as [4]:

$$H_{\mathrm{ex}} = -2\sum_{i,j} J_{a_i b_j}\left(\mathbf{s}_{a_i}\cdot\mathbf{s}_{b_j}\right) \tag{1}$$

The strength of the Coulomb interaction between these electrons is quantified by the so-called orbital exchange parameters $J_{a_i b_j}$ (off-diagonal components in the exchange-interaction matrix between the ground and the excited pair state) [5]. These have two different contributions: (i) the potential exchange, resulting from actual exchange interactions between the two electrons, and (ii) the kinetic exchange, originating from a one-electron-transfer process [24]. The former is always ferromagnetic, while the latter typically dominates in insulating systems of transition metal ions [24,25]. The kinetic exchange contribution is given by [26]:

$$J_{a_i b_j} = \frac{2}{n_{\mathrm{A}} n_{\mathrm{B}}}\frac{\left|\langle b_j|\hat{h}|a_i\rangle\right|^2}{U} \tag{2}$$

where n_{A} and n_{B} are the number of unpaired electrons in each ion. The electronic transfer integral $\langle b_j|\hat{h}|a_i\rangle$ in the numerator can be calculated [27] and is equivalent to the resonance integral in molecular orbital theory, with $\hat{h}$ being the one-electron Hamiltonian [24]. U is the energy, as defined in the Hubbard model [28], corresponding to the energy difference between the ground configuration and the electronic transfer configuration, when an electron transits from a to b, or vice versa. It can be assumed that the transfer integral is proportional to the overlap integral [29], $\langle b_j|\hat{h}|a_i\rangle \propto \langle b_j|a_i\rangle$, which qualitatively indicates the effects of the bridging geometry between the ions (specifically the superexchange angle), as it directly affects the overlap integral and, consequently, the value of the orbital exchange parameters.

Under certain conditions [2,30], such as when both ions are in their ground state (GS) and this state is not orbitally degenerate (although spin degeneracy is allowed), the interaction can be described [4,5] using the Heisenberg–Dirac–van Vleck Hamiltonian [31–33]:

$$H_{\mathrm{gs}} = -2J(\mathbf{S}_{\mathrm{A}}\cdot\mathbf{S}_{\mathrm{B}}) \tag{3}$$

where $\mathbf{S}_{\mathrm{A}}$ and $\mathbf{S}_{\mathrm{B}}$ are the total spin of each ion. Both the factor 2 and the sign vary depending on the convention adopted by different authors. Furthermore,

$$J = \frac{1}{4S_A S_B}\sum_{i,j} J_{a_i b_j} \tag{4}$$

is an effective value of the orbital exchange parameters, also known as the exchange coupling strength parameter [5]. The sign of J is determined by the type of interaction between the spins: $J > 0$ for ferromagnetic interaction and $J < 0$ for antiferromagnetic interaction [6]. Eq. (3) has been successfully used since the 1930s to describe properties of some magnetically ordered solids [34,35], as well as low-dimensional magnetic materials [36] and clusters of magnetic ions [37].

Theoretical models with more than one parameter are necessary when the orbital moment is not completely quenched [5]. Even in such cases, Eq. (3) is used as a first approximation and can reasonable describe the energy levels. The original form, Eq. (1), must be applied when characterizing transitions between different states of coupled ions [6]. The energy values (eigenvalues) associated with Eq. (3) are:

$$E(S) = -J\left[S(S+1) - S_{\mathrm{A}}(S_{\mathrm{A}}+1) - S_{\mathrm{B}}(S_{\mathrm{B}}+1)\right] \tag{5}$$

which depend on the total spin of the ion pair, $S = \{S_{\mathrm{A}} + S_{\mathrm{B}}, \ldots, |S_{\mathrm{A}} - S_{\mathrm{B}}|\}$, on the spins of each ion, and on the exchange coupling strength parameter, J. For each value of S, the ion pair system has an associated energy level, meaning that an energy splitting occurs due to the strength of the exchange coupling, which, in the case of the ground state, satisfies Landé's interval rule. Experimentally, deviations from Landé's pattern for the splitting have been observed [38], for which the Owen and Harris model [39] with a quadratic exchange Hamiltonian has been proposed, as a correction to Eq. (3):

$$H_{\mathrm{gs}} = -2J(\mathbf{S}_A\cdot\mathbf{S}_B) - j(\mathbf{S}_A\cdot\mathbf{S}_B)^2 \tag{6}$$

In most cases this term involves values of j two orders of magnitude smaller than J [5].

The effect of the splitting of states in exchange-coupled dimers is typically exemplified in the literature with the Mn^{2+} ion pair [4,5,7,12]. Mn^{2+} has an open-shell $3d^5$, with five unpaired electrons in the usual high-spin configuration. When the ion occupies a site in a crystal with O_h or T_d symmetry, the electronic terms of the free ion split as shown in the Tanabe–Sugano diagram for a $3d^5$ ion (Fig. 2a) [40].

When both ions are in their ground state, $^6A_1$, the operator in Eq. (3) can be applied. Since $S_A = S_B = 5/2$, the total spin values of the ion pair are $S = \{5, 4, 3, 2, 1, 0\}$. The levels into which the ground state of the pair, defined as the product function $\psi = |^6A_1, {}^6A_1\rangle$ (notation for the states of a dimer that will be used hereafter), splits are given by the collection of eigenvalues of Eq. (5):

$$E(S) = -J\left[S(S+1) - 35/2\right] \tag{7}$$

Fig. 2b reproduces the first experimental manifestation of the splitting in Mn^{2+} pairs, observed by McClure [12]. It can be seen how the energy levels of the dimer ground state are separated in energy proportionally to the total spin value, S, as indicated by Eq. (7) (Landé's interval rule).

When one of the ions is in an excited state, if this state is orbitally non-degenerate, such as $^4A_1$, the splittings in the dimer excited state $|^4A_1, {}^6A_1\rangle$ can also be obtained using Eq. (5). Fig. 2c exemplifies this, further showing the possible transitions between the dimer states, $|^6A_1, {}^6A_1\rangle \rightarrow |^4A_1, {}^6A_1\rangle$, whose selection rules will be discussed in the next section. However, for orbitally degenerate states, such as ^4E, the system $|^4E, {}^6A_1\rangle$ is better treated using the original Hamiltonian from Eq. (1).

1.2. The intensity mechanism for transitions between the electronic states of exchange-coupled ion pairs

Among all the spectroscopic effects mentioned above, the increase in the intensity of spin-forbidden bands, which also depends on the polarization of the electric field vector of the incident light [5], as well as the enhanced efficiency in upconversion processes in mixed TM/RE systems, find their theoretical framework in the works by Tanabe and collaborators [3,4,15].

Before introducing the Tanabe mechanism, it is worth recalling the selection rules and the mechanism by which spin-forbidden transitions can gain intensity in an individual ion that is not exchange-coupled. In this case, for d-d transitions to be allowed by the electric dipole mechanism, an odd-parity operator is required. Besides coupling with odd-parity phonons or the presence of a static odd crystal field created by the ligands, the exchange interaction relaxes the parity forbiddenness [5]. Although the single ion has a centrosymmetric coordination,

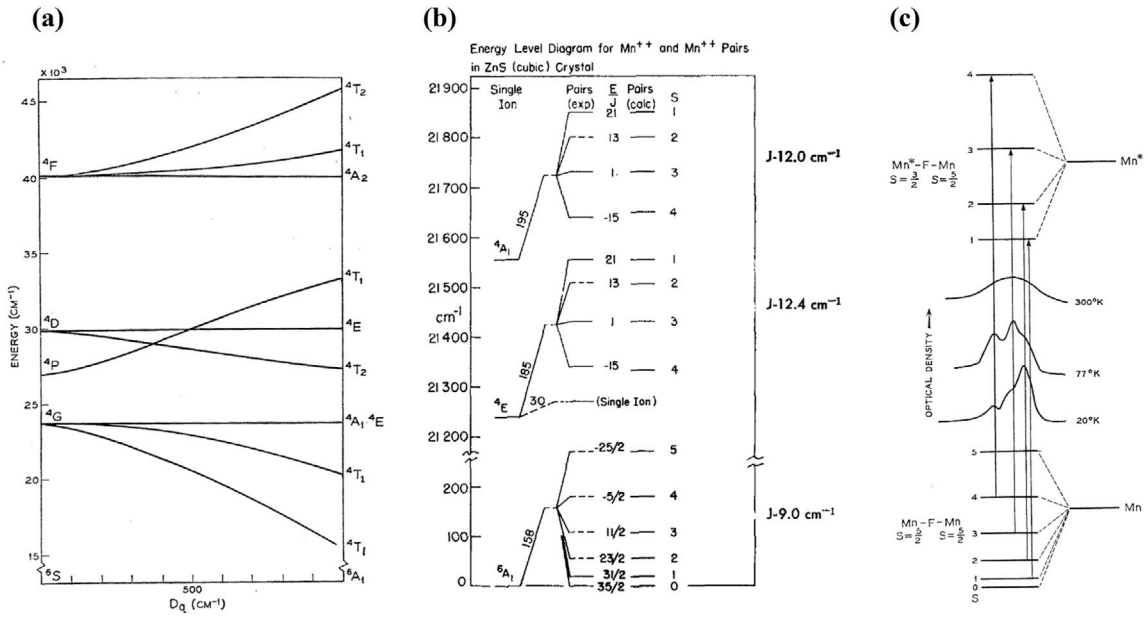

Fig. 2. **(a)** Tanabe–Sugano diagram for Mn^{2+} with $3d^5$ electronic configuration. **(b)** Diagram of experimental and calculated energy levels using the Heisenberg Hamiltonian for the individual ion (Mn^{2+}) and exchange-coupled pairs in ZnS:Mn^{2+}. Note that the levels of the dimer ground state follow Landé's interval rule (5:4:3:2:1:0) according to the value of S. **(c)** Temperature dependence of the transitions between the ground state $|^6A_1,^6A_1\rangle$ and the singly excited state $|^4A_1,\ ^6A_1\rangle$ of Mn^{2+} pairs (via the superexchange pathway Mn^{2+}-F^--Mn^{2+}) in the spectrum of $KZnF_3$:Mn^{2+}, along with the resulting split energy-level diagram. Note that the allowed transitions are those where the total spin of the dimer does not change, $\Delta S_{\text{dimer}} = 0$. The four lines are hot bands, as their intensity decreases with temperature until disappearing. Figures (a) and (c) reprinted from [4] ©1966 The Physical Society of Japan. Figure (b) reprinted from [12], with the permission of AIP Publishing.

this center of symmetry is broken within the pair by the presence of the neighboring ion. Additionally, spin–orbit coupling can be used to bypass the $\Delta S = 0$ restriction for spin-forbidden bands. In the case of dimers, they always experience an odd field created by the ligands, as they cannot occupy a center of symmetry like an individual ion might. Therefore, even in an exchange-coupled pair, the individual ion mechanism can allow a $\Delta S \neq 0$ transition, although it will not cause a significant difference compared to an individual ion under the influence of a similar field. Noting that the single-ion mechanism could not explain the effects observed on intensity, Ferguson et al. [4] questioned what specific mechanism the experimental data suggested, following Tanabe's formulation. The proposed mechanism starts from the interaction between the radiation field (**E**, **H**) and the pair of paramagnetic ions (A and B) as follows [4]:

$(\boldsymbol{\Pi} \cdot \mathbf{E})$(Scalar product of spin operators of ion A and B),

where $\boldsymbol{\Pi} = (\Pi_x, \Pi_y, \Pi_z)$ is a coupling constant (vector).

This means that a pair of ions can couple through the interaction with the electric field vector **E** of the incident light. The resulting interaction Hamiltonian, for a pair whose electrons are in the partially occupied orbitals a_i and b_j, is expressed as [4,5,41]:

$$H = \sum_{ij} (\boldsymbol{\Pi}_{a_i b_j} \cdot \mathbf{E})(\mathbf{s}_{a_i} \cdot \mathbf{s}_{b_j}) \tag{8}$$

The key property of the Tanabe mechanism is the spin-dependent nature of the transition dipole moment [42]:

$$\mathbf{P}^B_{\text{ex}} = \sum_{i,j} (\boldsymbol{\Pi}_{a_i b_j})(\mathbf{s}_{a_i} \cdot \mathbf{s}_{b_j}) \tag{9}$$

where B refers to the polarization of the light, and the components of the tensor $\Pi_{a_i b_j}$ are given by the derivative of the orbital exchange parameters, Eq. (2), with respect to each component of the electric field [4]:

$$\Pi^{\mu}_{a_i b_j} = \left(\frac{\partial J_{a_i b_j}}{\partial E^{\mu}} \right)_{E^{\mu} \to 0} \tag{10}$$

where $\mu = \{x, y, z\}$. In other words, accounting for the transition processes in dimers requires reconsidering the superexchange mechanism when an electric field is involved [43]. This indicates that wherever effective exchange pathways exist, the Tanabe mechanism operates effectively. The spin selection rules for the dimer in this mechanism are $\Delta S_{\text{dimer}} = 0$ and $\Delta M_S = 0$. Indeed, the orbital components of the dimer wavefunctions provide additional selection rules. For spin–flip transitions, such as the $^4A_2 \rightarrow {}^2E$ transition of Cr^{3+} or the $^6A_1 \rightarrow {}^4A_1, {}^4E$ transitions of Mn^{2+}, this mechanism proves to be the most efficient, rather than the individual ion mechanism previously discussed [5].

These selection rules are verified in the aforementioned Fig. 2c. Since the singly excited state $|^4A_1,^6A_1\rangle$ has total spin values $S^* = \{1, 2, 3, 4\}$, the selection rule $\Delta S_{\text{dimer}} = 0$ predicts that four lines will be observed. When the temperature is reduced, the population of the dimer ground state shifts to the lowest energy level, in this case with $S(|^6A_1,^6A_1\rangle) = 0$. As there is no analogous excited state with $S^* = 0$, at sufficiently low temperatures, the four lines will disappear. For this reason, these transitions are referred to as *hot bands* and are a key feature in the spectroscopy of exchange-coupled pairs. It is possible to determine Boltzmann populations for different values of J and compare them with the band areas at different temperatures. The effective J value, both for the ground and excited state, is known from the energy difference of the spectral lines [17].

2. Homonuclear transition-metal systems

2.1. Mn^{2+}–Mn^{2+}

Experimental results on the optical spectroscopy of exchange-coupled Mn^{2+} ions are collected in this section. Regarding optical absorption, most studies have already been compiled by McCarthy and Güdel [5]. They observed, as a function of temperature and applied external magnetic field, the excitation of Mn^{2+} pairs in the $^4A_1$(G), $^4T_2$(D), and ^4E(D) regions of the absorption spectrum of $CsMg_{1-x}Mn_xX_3$ (X = Cl, Br; $x = 0.04 - 0.20$). The ground-state exchange parameters for Mn-Br-Mn and Mn-Cl-Mn superexchange pathways were established at 14.2 cm^{-1} and 19.6 cm^{-1}, respectively. The values for the singly excited $^4A_1$ pair state were determined to be 18.6 and 26.8 cm^{-1} [17]. Fig. 3 reproduces a paradigmatic experiment on the 13 K absorption

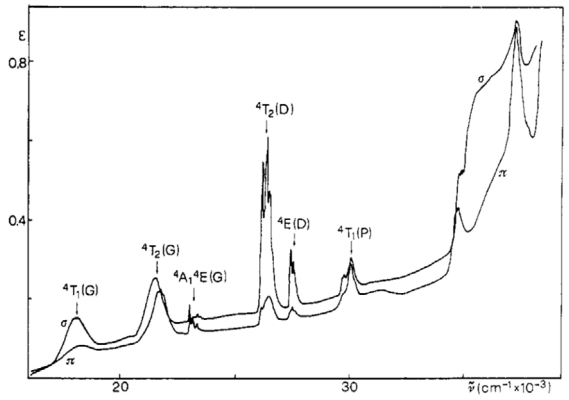

Fig. 3. 13 K polarized optical absorption spectrum of the $CsMg_{0.80}Mn_{0.20}Br_3$ single crystal. All the observed transitions are spin-forbidden; however, the exchange coupling mechanism in Mn^{2+} pairs enhanced them by one to two orders of magnitude compared to the isolated ion. Reprinted with permission from McCarthy and Güdel [17]. Copyright (1984) by the American Chemical Society.

spectrum of the $CsMgBr_3$ single crystal doped with 20% Mn^{2+}. The absorptions due to electronic transitions in Mn^{2+} pairs are between one and two orders of magnitude greater than those of the individual ion, and moreover, the intensity of some of the transitions (e.g., to $^4T_1$(G) or $^4T_2$(D)) strongly depends on the polarization of the electric field (π and σ correspond to **E** parallel and perpendicular to the Mn-X-Mn pathway, respectively).

2.1.1. Exchange coupling effects on the emission spectrum (exchange-induced luminescence)

The luminescence of slightly Mn^{2+}-doped samples originates from the spin-forbidden transition $^4T_1 \rightarrow {}^6A_1$, resulting in a long luminescent lifetime, typically in the 10–100 ms range in centrosymmetric monomers [44,45].

The luminescent properties of ion pairs differ significantly from those of individual ions due to processes such as energy transfer within the pair [46] or interactions that cause shifts in energy levels [47]. These differences are of both theoretical and practical interest, particularly in applications involving interactions between optically active ions [7]. However, the long emission lifetime of Mn^{2+} can present challenges for some applications [48].

Regarding the luminescence of Mn^{2+} pairs, the studies conducted range from time-resolved emission spectroscopy in $ZnS:Mn^{2+}$ [49] to time-resolved magnetophotoluminescence of colloidal $ZnSe:Mn^{2+}$ quantum dots [50]. Passing through the studies [7,42,51] in which two of the most relevant results observed in the emission of Mn^{2+} coupled pairs are shown and explained: (i) the redshift in the emission, and (ii) the shortening of the luminescent lifetime due to the exchange coupling relaxing the spin selection rule, both when increasing the concentration of Mn^{2+} in different lattices [42,51,52]. These two aspects are shown separately below.

Recently, several authors have reported near-infrared (NIR) luminescence in pure Mn^{2+} or heavily Mn^{2+}-doped host lattices, attributing it to Mn^{2+}-Mn^{2+} pair emission, in addition to the well-known green–red emission from isolated Mn^{2+} ions, depending on coordination symmetry [53–56]. However, Meijerink and co-workers [57] have proposed a different and more compelling explanation based on experimental observations, including the dependence of luminescence on concentration and temperature, and also supported by archival literature. For instance, the exceptionally large redshifts — up to 7,000 cm^{-1} — reported for exchange-coupled Mn^{2+}-Mn^{2+} pairs in α-MnS [53] significantly exceed what would be expected for typical Mn^{2+} pairs. Moreover, the excitation spectra for both the visible and NIR emissions exhibit the same excitation profile, indicating a Stokes shift greater than 8,200 cm^{-1}, from approximately 640 nm (the maximum of the lower absorption band) to 1360 nm (the maximum of the NIR emission). This evidence strongly contradicts the assignment of the NIR emission to Mn^{2+} dimers. Instead, a more plausible origin for this emission is a thermally activated energy transfer from excited Mn^{2+} ions to unidentified NIR-emitting defect or impurity centers, as was proposed by Meijerink and co-workers [57].

It is essential to evaluate the presence of impurities in the starting materials and throughout any stage of the synthesis process. If these potential sources of contamination are ruled out, luminescent impurities may still arise from different oxidation states of Mn, which are often influenced by the synthesis method and processing temperatures.

(i) Redshift luminescence upon increases in the Mn^{2+} concentration. Barthou et al. [51] explored the optical properties of $Zn_2SiO_4:Mn^{2+}$ using selective pulsed photon excitation. Their study identifies a correlation between the luminescence associated with the $^4T_1 \rightarrow {}^6A_1$ transition and the relative concentration of isolated Mn^{2+} ions *versus* pairs of Mn^{2+} ions within the material structure. In the Zn_2SiO_4 (willemite, space group $R\bar{3}$) lattice, Mn^{2+} ions replace Zn^{2+} at two distinct sites, both surrounded by oxygen ions in a slightly distorted tetrahedral (T_d) arrangement. At low temperatures and concentrations, the zero-phonon lines associated with these two inequivalent crystallographic sites are separated by 410 cm^{-1} [58]. Fig. 4a reproduces the luminescence spectra of $Zn_2SiO_4:Mn^{2+}$ as a function of concentration. It revealed two bands centered at 519 nm and 526 nm. As the concentration of Mn^{2+} increases, a redshift in the Mn^{2+} emission band was observed. This behavior was attributed to the formation of Mn^{2+} pairs as the concentration increases, a phenomenon also reported in $CaS:Mn^{2+}$ and $SrS:Mn^{2+}$ [59]. Another evidence for this redshift comes from Vink et al. [7], who investigated the luminescence spectra of Mn^{2+}-doped $MgAl_2O_4$ at different concentrations (0.2, 2, and 5 mol%). The observed spectra revealed a redshift in the emission wavelength, shifting from 518.8 nm at lower Mn^{2+} concentrations to 528.3 nm at 10% Mn^{2+} (Fig. 4b). This shift corresponds to an energy change of 350 cm^{-1}, which is slightly greater than the redshift of 250 cm^{-1} previously observed for Mn^{2+} in Zn_2SiO_4 [51].

Ronda and Amrein [42] revisited the Mn^{2+} luminescence redshift phenomenon. While Barthou et al. [51] associated the shift with the formation of Mn^{2+} ion pairs without a fundamental explanation, Ronda and Amrein [42] attributed this redshift to the exchange interactions between the Mn^{2+} ions, showing that the observed redshift is linked to variations in the exchange coupling when both Mn^{2+} ions are in the ground state (with J being the effective exchange parameter) compared to when one ion is excited (with J^* being the effective exchange parameter of this singly excited state). Fig. 4c reproduces the calculation of the luminescence redshift at different total spin values in the excited state, S^*, as a function of the J^*/J ratio [42]. The antiferromagnetic nature of the exchange interaction of Mn^{2+} ($J < 0$) generally leads to a blueshift when forming ion pairs. However, Ferguson et al. [4] pointed out that if the exchange interaction is stronger in the excited state than in the ground state, the energy splitting is larger and the emission from the low lying dimer levels induces a redshift in the emission spectrum. According to calculations by Ronda and Amrein [42], whenever $J^*/J > 1.56$, the redshift effect will occur. They also noted that for significant exchange coupling (large values of J), the magnitude and direction of the shift could depend on the temperature by thermal population of dimer levels. If the exchange interactions in the ground state and the excited state were equal ($J^* = J$), the emission energy remained unchanged by temperature or the concentration of Mn^{2+}.

(ii) Shortening of the luminescent lifetime with the increase in Mn^{2+} concentration. Stevels and Vink [52] determined that in Zn_2SiO_4 doped with Mn^{2+}, decay times of around 12 ms and 15 ms at 1.6 K are linked to two distinct Mn sites. As Mn^{2+} concentration increases, additional zero-phonon lines appear. Their intensity scales with the Mn content,

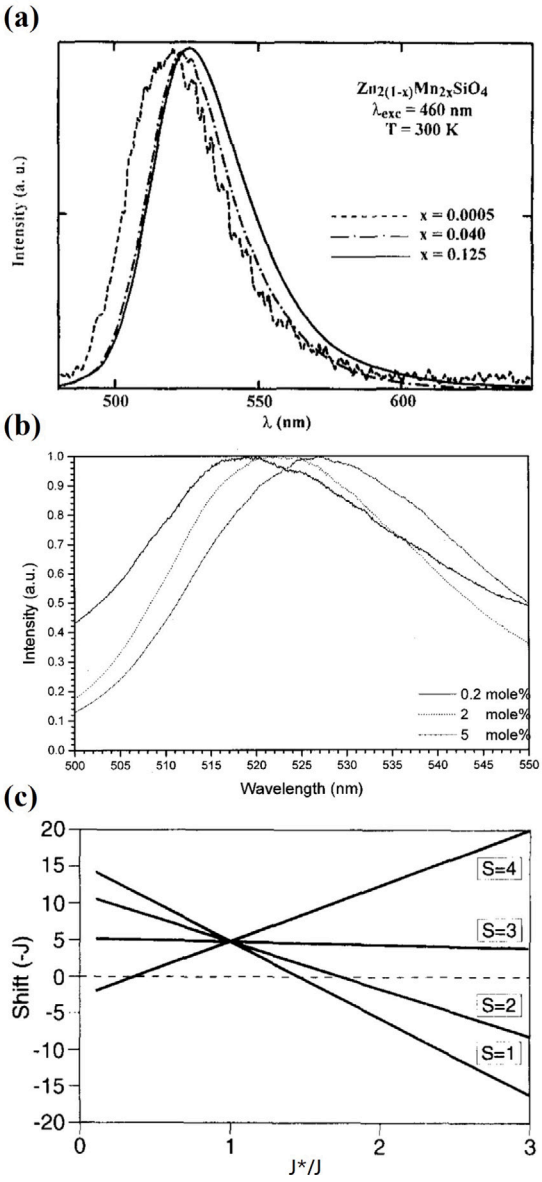

Fig. 4. Emission spectra of **(a)** Zn_2SiO_4:Mn^{2+} and **(b)** $MgAlO_4$:Mn^{2+}, as a function of Mn^{2+} concentration. **(c)** Calculation of the exchange-induced shift in the emission bands of Mn^{2+} pairs, from the singly excited state with spin S^*, as a function of the ratio between the exchange parameter of the singly excited state (J^*) and that of the pair ground state (J). Figure (a) reprinted from Barthou et al. [51] and (b) from Vink et al. [7]. Copyright The Electrochemical Society. Reproduced by permission of IOP Publishing Ltd. All rights reserved. Figure (c) reprinted from Ronda and Amrein [42]. Copyright (1996), with permission from Elsevier.

indicating ion pair formation at higher concentrations. Barthou et al. [51] further investigated this behavior by recording normalized decay curves under pulsed excitation, between 519 and 526 nm (Fig. 5a). They identified non-exponential decays and a rapid component outside the scope of the $^4T_1 \rightarrow {}^6A_1$ transition, suggesting complex relaxation pathways. These findings were explained by distinguishing between original centers (isolated Mn^{2+}) and new centers (forming at higher Mn content), with the latter showing oscillator strengths roughly nine times larger. Since lifetime is inversely proportional to the oscillator strength in pure radiative transitions, an increase in oscillator strength with increased Mn^{2+} content yields shorter lifetimes in dimers in comparison to monomers. The shortening of the lifetime at higher concentrations can also be attributed to concentration quenching; however, in this case, the luminescence intensity should decreases with Mn concentration.

Subsequent work by Vink et al. [7] showed that in Mn^{2+}-doped $MgAl_2O_4$ at low doping levels, Mn^{2+} luminescence follows a single exponential decay (Fig. 5b). With increasing Mn concentration, faster and non-exponential decays set in, caused by Mn^{2+} pairs that display shorter lifetimes. In Mn^{2+}-doped $MgAl_2O_4$, the lifetime decreases from 7.2 ms to 4.5 ms, which is notably less drastic than the drop from 15 ms to 1.8 ms in other lattices like Zn_2SiO_4:Mn^{2+}. The difference stems from reduced exchange coupling, given that the spinel phases $MgAl_2O_4$ and $ZnGa_2O_4$ exhibit larger Mn–Mn spacings than Zn_2SiO_4, resulting in gentler decreases in lifetime [7]. Exchange interactions, also responsible for the redshift of Zn_2SiO_4:Mn^{2+} emission at elevated Mn contents, need to be examined with more sophisticated treatments — incorporating higher-order exchange terms or spin–orbit coupling — to achieve a deeper quantitative picture [42]. Besides exchange interactions, the spinel can accommodate the Mn^{2+} in two sites: tetrahedral (Mg) and octahedral (Al), the latter requiring charge compensation. This rich variety of centers and superexchange pathways among them makes it a complex system, still deserving a thoroughly structural characterization.

2.1.2. The luminescent $|^4T_1, {}^6A_1\rangle$ singly excited state: a longstanding question

The photoswitchable magnetic behavior observed by Bradshaw et al. [50] in ZnSe:Mn^{2+} quantum dots — where Mn^{2+}-Mn^{2+} dimers transition from an antiferromagnetic ground state ($S = 0$) to a ferromagnetic excited state ($S = 4$) — highlights the potential for optically controlling spin in doped semiconductor systems. In II–VI and III–V semiconductors, nearest-neighbor Mn^{2+}-Mn^{2+} pairs typically adopt an $S = 0$ ground-state configuration, reducing both the overall magnetization [60,61] and the fraction of Mn^{2+} centers available to interact with free carriers [61]. These effects limit the range of possible magneto-optical and spintronic applications.

Moreover, work by Viswanatha et al. [62] revealed that, at higher dopant concentrations, the circular polarization of Mn^{2+} *d-d* emission intensity diminishes, indicating that isolated monomeric Mn^{2+} ions are the primary contributors to magnetically polarized photoluminescence. Despite the importance of understanding dimer excited states for interpreting how doping affects magnetoluminescence, direct experimental evidence is still deserving.

Earlier findings from McClure [12] on $Zn_{1-x}Mn_xS$ associated sharp zero-phonon absorption features in heavily doped samples with ferromagnetic exchange coupling in the excited state ($|{}^6A_1, {}^6A_1\rangle \rightarrow |{}^4E, {}^6A_1\rangle$). However, Langer and Ibuki [63] questioned this interpretation, suggesting that phonon interactions might be responsible. Subsequently, Busse et al. [49] used time-gated photoluminescence to identify short-lived emission lines originating in Mn^{2+}-Mn^{2+} dimers, which appeared to preserve an antiferromagnetic arrangement in their excited state.

Using time-resolved magnetophotoluminescence spectroscopy, Bradshaw et al. [50] showed that Mn^{2+}-Mn^{2+} dimers in colloidal $Zn_{1-x}Mn_xSe$ nanocrystals can be isolated from their monomer counterparts. This distinction hinges on the Tanabe mechanism, which leads to shorter luminescence decay times for dimers, thereby enabling a separate examination of their magneto-optical response. Such measurements further revealed that the magnetic circular polarized luminescence (MCPL) from these dimers reaches saturation at magnetic fields lower than those required for monomers, consistent with a high-spin ($S = 4$) ferromagnetic configuration in the excited state.

In addition, the dimer luminescence under full magnetic saturation exhibited nearly complete (~ 100%) circular polarization, in contrast to approximately 40% for Mn^{2+} monomers [50]. This discrepancy arises from the distinct $\Delta m_s = \pm 1$ transitions available to the dimer excited state compared to the monomer. Theoretical insights from perturbation theory and density functional theory (DFT) suggest that ferromagnetic

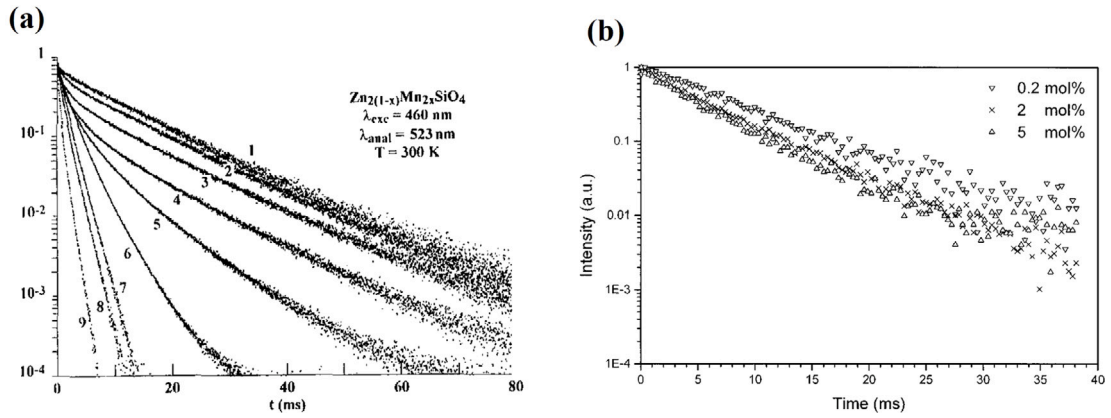

Fig. 5. Normalized decay curves of the emission in **(a)** Zn_2SiO_4:Mn^{2+} and **(b)** $MgAl_2O_4$:Mn^{2+} measured at room temperature and as a function of the concentration of the Mn^{2+} dopant ion. Both show a decrease in the lifetime as the concentration increases (i.e., the formation of Mn^{2+}-Mn^{2+} pairs). Figure (a) reprinted from Barthou et al. [51]. Copyright (1994) The Electrochemical Society. Figure (b) reprinted from Vink et al. [7]. Copyright (2001) The Electrochemical Society. Reproduced by permission of IOP Publishing Ltd. All rights reserved.

exchange in the $|^4T_1, {}^6A_1\rangle$ excited state results from a dominant single orbital superexchange pathway. These findings [50] settle a longstanding question regarding the exchange coupling mechanism in excited Mn^{2+}-Mn^{2+} dimers and propose novel routes for manipulating spin optically in semiconductor systems of practical importance.

(i) The sign and purity of the Mn^{2+}–Mn^{2+} dimer magnetic circularly polarized luminescence. Fig. 6 provides a schematic overview of how a purely σ^+ polarized response emerges [50]. In a simplified cubic, spin-only framework, Mn^{2+} monomers at low temperature emit photons primarily from the $m_s = -3/2$ Zeeman sublevel of the excited $^4T_1$ state. Within the Faraday geometry, selection rules allow only $\Delta m_s = \pm 1$, producing right (σ^+) and left (σ^-) circularly polarized emissions. Therefore, the MCPL ratio for monomers depends on the competing probabilities of the $m_s = -3/2 \rightarrow -5/2$ (σ^-) and $m_s = -3/2 \rightarrow -1/2$ (σ^+) transitions, which are unequal for deeper physical reasons [50,64].

In contrast, in Mn^{2+}–Mn^{2+} exchange-coupled pairs, the total luminescence is primarily governed by spin-allowed ($\Delta S = 0$) steps within the spin-ladder of the dimer, consistent with the Tanabe mechanism [3,4,15]. As shown in Fig. 6 [50], ferromagnetically coupled dimers ($S = 4$) emit mainly through transitions between the $S = 4$ excited state and the $S = 4$ ground state. Because the fully magnetized dimer excited state corresponds to $m_s = -4$, and there is no $m_s = -5$ sublevel available, only a $\Delta m_s = +1$ process can occur, producing exclusive σ^+ circularly polarized light. Hence, the dominance of $\Delta S = 0$ dimer transitions leads to a purely σ^+ MCPL for the coupled Mn^{2+}–Mn^{2+} pair.

Although the real luminescent excited states in both monomers and dimers are more intricate due to Jahn–Teller distortions and spin–orbit coupling, these spin-only diagrams capture the essential physics revealed by the experimental measurements [50].

(ii) The sign of Mn^{2+}–Mn^{2+} dimer excited-state superexchange coupling. Bradshaw et al. [50] argue that the photoexcitation-induced inversion of the Mn^{2+}-Mn^{2+} dimer exchange coupling can be explained by assessing the distinct superexchange pathways in both the ground and excited states. Fig. 7a [50] offers a schematic of two tetrahedrally coordinated Mn^{2+} ions, each initially in the $^6A_1$ ground state ($|^6A_1, {}^6A_1\rangle$) where all five *d* orbitals on each ion are singly occupied. Under these conditions, spin transfer between the ions depends on having opposite spins, thus giving rise only to antiferromagnetic interactions. In contrast, the luminescent dimer excited state ($|^4T_1, {}^6A_1\rangle$) is characterized by one Mn^{2+} center adopting an $e^3t_2^2$ arrangement, leaving a vacant t_2 orbital and a doubly filled e orbital. Spin transfer from a

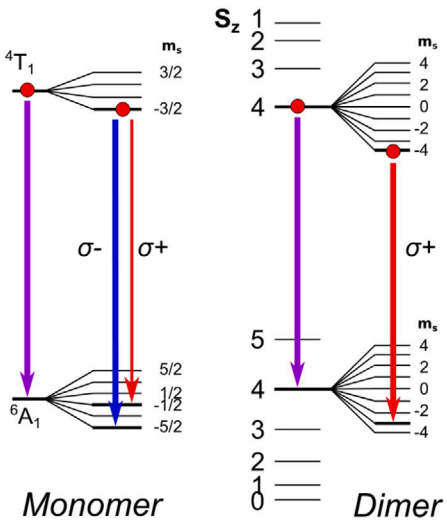

Fig. 6. In a simplified spin-only framework, schematic diagrams highlight how MCPL is established for both monomers and dimers in $Zn_{1-x}Mn_xSe$ and analogous systems. On the monomer side (left), the circular polarization depends on the balance between the transition moment strengths for $\Delta m_s = -1$ (σ^-, indicated by a blue arrow) and $\Delta m_s = +1$ (σ^+, shown with a red arrow). In contrast, the dimer (right) features an antiferromagnetically coupled ground state paired with a ferromagnetically coupled excited state. Luminescence is then dominated by spin-allowed ($\Delta S = 0$) transitions, within which only the $\Delta m_s = +1$ (σ^+) pathway conserves angular momentum. As a result, the dimer exhibits a fully σ^+-polarized emission whose overall sign is reversed relative to the monomer behavior. The energy separations displayed in the figure are not to scale. Reprinted with permission from Bradshaw et al. [50]. Copyright (2014) by the American Physical Society.

half-occupied *d* orbital into this unoccupied t_2 orbital stabilizes parallel (ferromagnetic) spin alignment, depicted by the thick blue arrow in Fig. 7a [50]. A similar effect arises from the transfer of spin from the doubly populated e orbital to a half-filled orbital on the other Mn^{2+} ion (indicated by the thin blue arrow), reinforcing ferromagnetic behavior. Meanwhile, additional antiferromagnetic routes akin to the ground state remain possible (dashed arrows). Because both ferromagnetic and antiferromagnetic channels exist in the excited state, the overall sign of the exchange coupling depends on their relative magnitudes and on the degree of *d*-orbital overlap with the bridging Se^{2-} anion. The observation that the net exchange coupling becomes ferromagnetic in

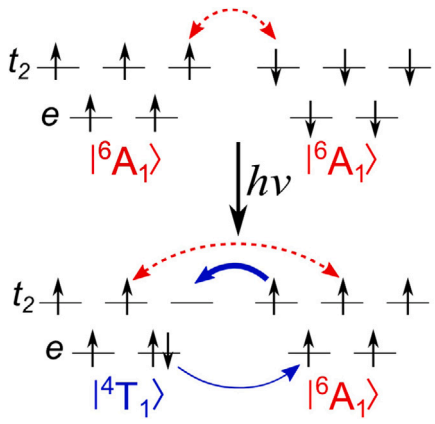

Fig. 7. Diagram summary of spin-transfer pathways that underlie both ground- and excited-state magnetic exchange coupling in ZnSe dimers containing Mn^{2+} ions. The dashed red arrows stand for antiferromagnetic contributions, while the solid blue arrows indicate ferromagnetic interactions. Reprinted with permission from Bradshaw et al. [50]. Copyright (2014) by the American Physical Society.

the luminescent excited state has led to the conclusion that the vacant t_2 orbital must exhibit strong overlap with Se^{2-}, the mediator of these superexchange processes [50].

2.1.3. Exchange effects on the absorption and exciton dynamics in the 1D $[(CH_3)_4N]MnCl_3$

In most concentrated transition-metal (TM) halides and oxides, visible-near-infrared photoluminescence (PL) at ambient conditions is typically quenched due to energy transfer between TM ions (migration). This excitation migration and its subsequent trapping at non-PL impurities or intrinsic defects is a phenomenon commonly referred to as concentration quenching [6].

In these TM compounds, the ground-state to excited-state transition mechanism and energy transfer between TM ions are mediated by exchange coupling. An increase in the exchange interaction enhances both the transition probability for exciton creation (Mn^{2+} excited state) and transfer probability. Exciton creation in this scenario refers to the excitation of Mn^{2+} from the $^6A_1$(S) ground state to the $^4T_1$(G) excited state. Within a single ion, the excited state forms a localized excitation in the lattice. Depending on the system dimensionality (1D, 2D or 3D), this exciton can migrate via energy transfer to neighboring Mn^{2+} ions, favoring the excitation transport. Understanding which process is most sensitive to the exchange interaction is crucial for determining whether an increase in this interaction favors PL efficiency or trapping at non-PL centers. This knowledge is critical for developing strategies to design highly efficient PL TM-concentrated compounds. Interestingly, for a given concentration of non-radiative impurities or defects (N), the probability of exciton trapping exhibits a strong dependence on the crystal dimensionality. The number of steps (Mn–Mn hopping processes) required for the exciton to reach a non-PL center (killer) is proportional to $N^{1/n}$, with $n = 1, 2$, or 3, being the crystal dimensionality. This holds true regardless of whether the energy-transfer process is a random walk or an exciton-driven motion. Consequently, the time to reach a non-PL center decreases drastically when passing from 1D to 2D and 3D systems. Therefore, the probability of reaching an impurity via either process is lowest in 1D systems, making room-temperature PL in 1D TM-concentrated compounds more likely.

Based on these conditions, the 1D $(CH_3)_4NMnCl_3$ (TMMC) crystal emerges as a highly efficient PL material at ambient conditions. Its linear chain crystal structure, shown in Fig. 8a, consists of face-sharing $[MnCl_6]^{4-}$ octahedra with D_{3d} symmetry. These chains are interconnected by $(CH_3)_4N^+$ cations, resulting in a $P6_3/m$ crystal structure [65,66], and establishing it as an ideal 1D system of exchange-coupled Mn^{2+} ions. The intra-chain Mn–Mn exchange interaction is an order of magnitude greater than the inter-chain Mn–Mn interaction [66].

Extensive research has focused on modifying the TMMC structure to enhance its PL efficiency [66–70]. Exciton migration within these systems is well described by an exchange-assisted Mn–Mn hopping mechanism, akin to a random walk process. The presence of non-PL exciton traps or barriers for exciton migration significantly impacts the PL, either quenching it entirely or enhancing it, as demonstrated by Knochenmuss and Güdel [69] through Cu^{2+} and Cd^{2+} doping in TMMC, respectively.

Correlation studies examining structural, magnetic and optical properties in TMMC under high-pressure conditions [66] reveal that crystal compression is anisotropic, with the $MnCl_6$ center experienced increasing axial distortion along the chain (hexagonal c axis) with hydrostatic pressure. This structural variation promotes an increase in the crystal-field strength at Mn^{2+} and a splitting of the $^4T_1$ emitting state, leading to large PL pressure shifts. This makes TMMC a promising candidate for highly sensitive low-pressure sensor with significant interest in bioscience and biotechnology [71].

Herein, how the increase of Mn–Mn exchange interaction by applying hydrostatic pressure can enhance or reduce the PL of TMMC was investigated. The effects of exchange interaction on the optical properties has been studied by optical absorption and time-dependence PL [72]. Fig. 8b illustrates the pressure dependence of the optical absorption spectrum of TMMC. The spectrum exhibits five crystal-field bands attributed to intraconfigurational transitions within the $3d^5$ configuration of Mn^{2+} in a nearly octahedral symmetry (D_{3d}). These bands exhibit a redshift with increasing pressure, consistent with an increase of $10Dq$ and a reduction of the B and C Racah parameters due to enhanced covalency under pressure [72]. Notably, the band intensity (oscillator strength, $f \sim 10^{-5}$) increases with pressure, reaching three times the ambient pressure intensity at 10 GPa (Figs. 8b,c). The oscillator strength, $f(P)$, shows a linear dependence on pressure, with a relative variation being 0.20 GPa^{-1}. Interestingly, the measured pressure coefficient aligns well with the variation of the exchange coupling, J, determined by magnetic measurements under pressure [66,72]. This concurrence suggests that the spin-forbidden crystal-field transitions, $^6A_1 \rightarrow {}^4\Gamma_i$ ($\Gamma_i = T_1, T_2, E$ and A_1), are activated via exchange interactions. This behavior of the oscillator strength with pressure contrasts with that observed for Mn^{2+} impurities in centrosymmetric sites. In these systems, the oscillator strength of d-d transitions decreases with pressure due to increase in the odd-parity vibration frequency and an increased separation of the feeding charge-transfer states, both of which diminish the vibronic mechanism [73].

The pressure-induced exchange enhancement has significant consequences for the PL lifetime. The increase in oscillator strength and Mn–Mn hopping rate, both yield shorter lifetimes. The increase in oscillator strength and Mn–Mn hopping rate both contribute to shorter lifetimes. While hopping primarily affects the exciton trapping time, which decreases with the non-radiative impurity concentration (e.g., $[Cu^{2+}]$), the increase in oscillator strength enhances radiative probability, also reducing the PL lifetime.

Fig. 9a shows the PL time dependence, $I(t)$, for TMMC corresponding to the red emission band at 633 nm. The semilogarithmic plot of $I(t)$ versus t clearly demonstrates the lifetime decrease with pressure. This decreases further evident in Fig. 9b where the average lifetime, calculated using the equation

$$\tau = \frac{\int_0^\infty tI(t)dt}{\int_0^\infty I(t)dt} \tag{11}$$

is plotted as a function of pressure.

The $\tau(P)$ behavior can be described using a random walk model for the Mn–Mn hopping with the equation [72]:

$$\tau^{-1}(P) = \tau_{rad}^{-1}(P) + (2x)^2\tau_{Mn-Mn}^{-1}(P) \tag{12}$$

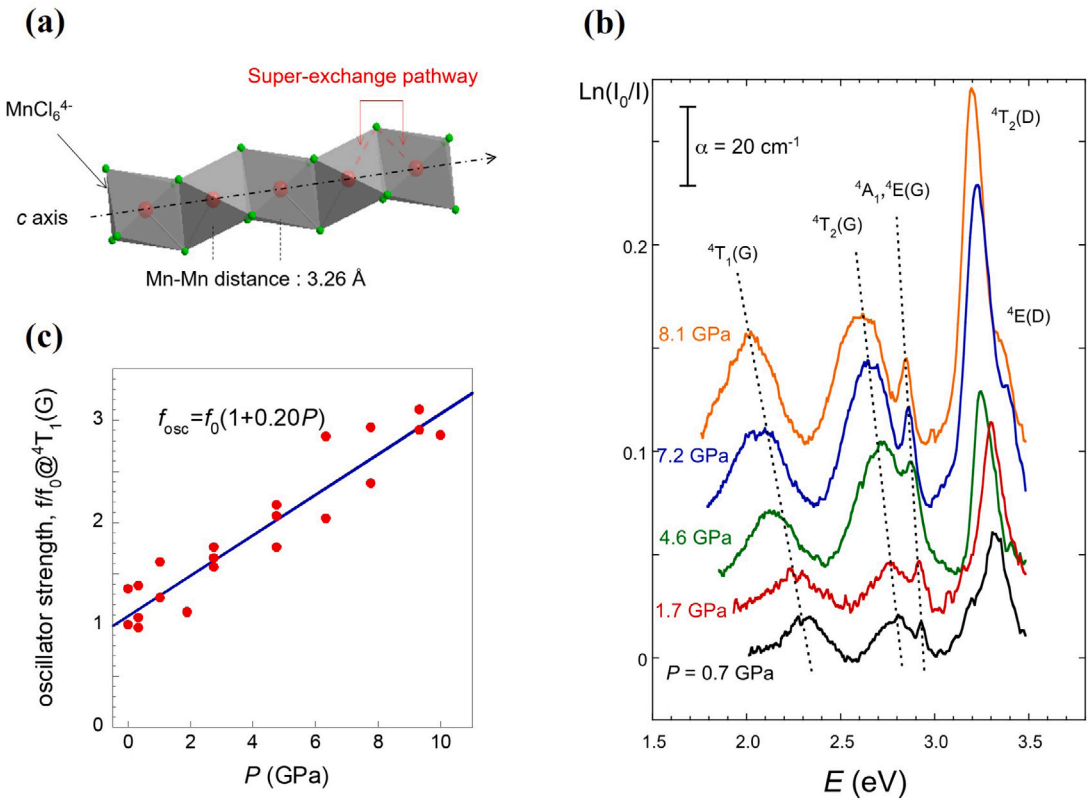

Fig. 8. **(a)** Crystal structure of $N(CH_3)_4MnCl_3$ (TMMC), showing the inorganic linear chains of face-sharing sixfold coordinated Mn^{2+} (D_{3d}). **(b)** Pressure dependences of the TMMC absorption spectra. **(c)** $^4T_1(G)$ oscillator strength derived from the absorption band area. Data are normalized to sample dimensions through the TMMC equation of state [66]. Note the oscillator strength enhancement of all transitions with pressure consistently with an increase of the exchange interaction induced by pressure.

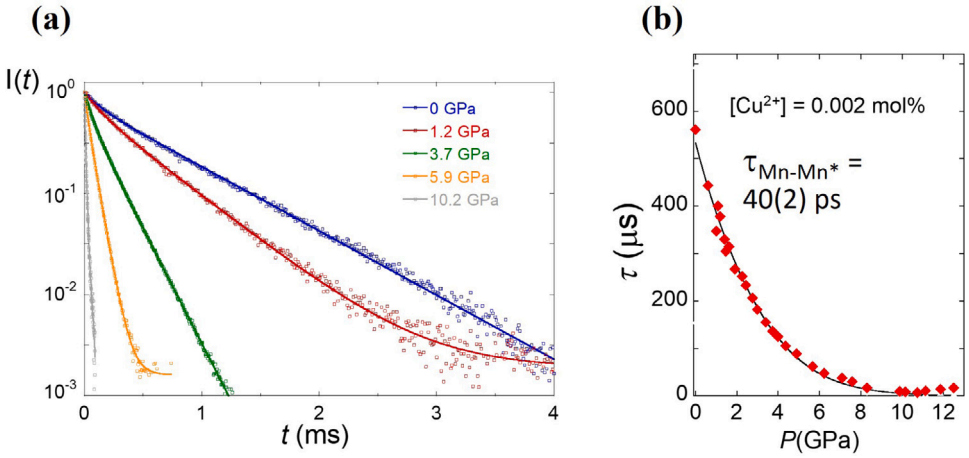

Fig. 9. **(a) (b)** Pressure dependencies of the TMMC PL lifetime. The decrease in lifetime with pressure is due to the increase in energy transfer probability caused by the increase of exchange interaction with pressure.

Here, x represents the molar concentration of Cu^{2+}, which is 2×10^{-5}, $\tau_{rad}(0) = 0.8$ ms (derived from pure TMMC), and

$$\tau_{rad}^{-1}(P) = \tau_{rad}^{-1}(0)\frac{f}{f_0} \tag{13}$$

with $\frac{f}{f_0} = 1 + 0.2P$ [72]. The theoretical $\tau(P)$ curve was obtained using a hopping time at ambient pressure $\tau_{Mn-Mn}(0) = 40$ ps.

This analysis of the excited-state dynamics suggests that applying pressure, and thus increasing the Mn–Mn exchange coupling along the chain, leads to an increase in the PL quantum yield. However, for samples containing non-radiative impurities (Cu^{2+}), the PL intensity decreases above a critical pressure that decreases with the impurity concentration (x) [72]. For $x > 10^{-3}$ the PL is practically quenched and any remaining PL decreases with pressure due to dominance of trapping to non-radiative impurities.

2.2. Mn^{3+}–Mn^{3+}

2.2.1. *Exchange effects on the spin–flip electronic transitions in Jahn–Teller Mn^{3+} fluorides. Structural correlations*

Mn^{3+} fluorides with the general formula A_nMnF_m (where A is a monovalent cation, $n = 1, 2, 3$, and $m = n + 3$) exhibit a diverse range of perovskite-type crystal structures. These structures are significantly

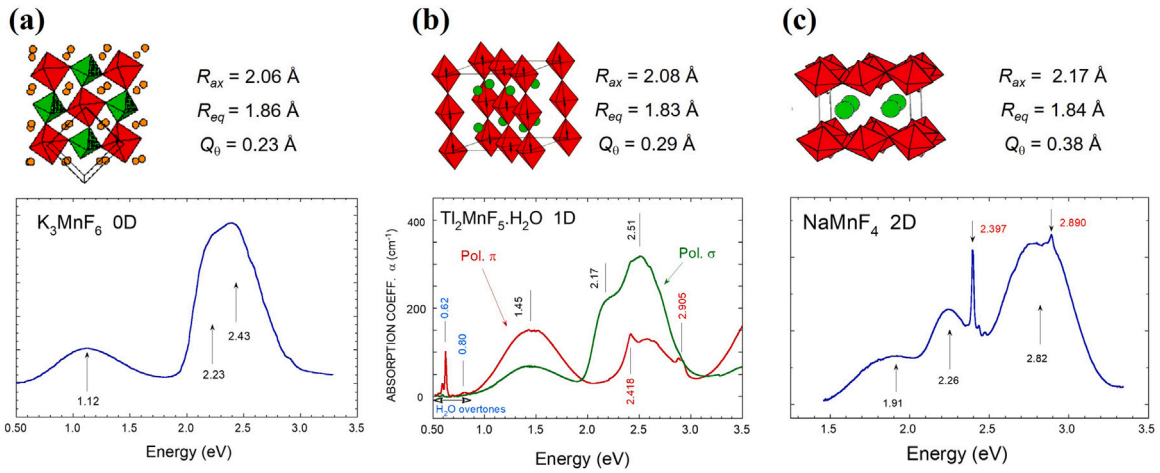

Fig. 10. Variation of the optical absorption spectrum of single crystal of Mn^{3+} fluorides with different dimensionality: **(a)** K_3MnF_6 (0D); **(b)** $Tl_2MnF_5{\cdot}H_2O$ (1D); and **(c)** $NaMnF_4$ (2D). A schematic view of the crystal structure and associated parameters for MnF_6 are given on the top side [74,80]. The 1D $Tl_2MnF_5{\cdot}H_2O$ crystal habit allows us to measure the polarized spectra with the light electric vector parallel (π) and perpendicular (σ) to the edge-sharing MnF_4F_2 chains, respectively. The spectra consist of three broad bands associated with one electron spin-allowed transitions within the nearly D_{4h} MnF_6 complex (transition energies are in eV), while the narrow peaks around 2.4 and 2.9 eV correspond to spin–flip transitions within the $3d^4$ electron configuration. Note that the broad band energies and the associated $3d$-orbital splitting strongly depend on the D_{4h} distortion described by the normal coordinate Q_θ. The spin–flip peak intensity strongly depends on the exchange interaction, being maximum in 2D, weaker in 1D, arationalizend not observed in 0D. These transitions are polarized along the Mn-F-Mn superexchange direction (along the chain), consistent with selection rules for exchange-induced transitions [79].

influenced by the Jahn–Teller (JT) effect of the Mn^{3+} ion ($3d^4$) [74–81].

Depending on the ligand sharing between $[MnF_6]^{3-}$ units, the crystal structure shows different dimensional arrangements. As shown in Fig. 10, isolated $[MnF_6]^{3-}$ units (as in K_3MnF_6) result in a 0D structure. Sharing two axial ligands leads to 1D linear chains (e.g., $Tl_2MnF_5{\cdot}H_2O$) [82], while sharing four ligands within a plane results in 2D layers (e.g., $NaMnF_4$) [83]. In all these compounds, the local structure of the $[MnF_6]^{3-}$ units adopts an elongated, nearly tetragonal (D_{4h}) geometry due to the combined effect of the JT effect and crystal anisotropy.

While the Mn-F bond lengths are similar, the tetragonal distortion increases with the crystal dimensionality. This distortion can be quantified by measuring the tetragonal normal coordinate $Q_\theta = \frac{2}{\sqrt{3}}(R_{ax} - R_{eq})$, where R_{ax} and R_{eq} are the long Mn-F distance and the average short Mn-F distances, respectively. This tetragonal distortion splits the parent octahedral $e_g(3z^2 - r^2, x^2 - y^2)$ and $t_{2g}(xy, yz, xz)$ orbitals into $b_{1g} + a_{1g}$ and $b_{2g} + e_g$ sets, respectively. This can be observed spectroscopically as three broad spin-allowed bands in the absorption spectra, assigned to transitions $^5B_{1g} \rightarrow {}^5\Gamma_i$ ($\Gamma_i = A_{1g}, B_{2g}, E_g$) in order of increasing energy (Figs. 10 and 11). Notably, the transition energies provide direct information on $10Dq$, Δ_e, and Δ_t (see orbital level diagram in Fig. 11), allowing for the determination of the electron–lattice couplings associated with the JT effect [74,80].

Additionally, spin-forbidden transitions ($^5B_{1g} \rightarrow {}^3B_{1g}$) can be observed in the absorption spectra. These are spin–flip transitions within the $3d^4$ configuration keeping the orbital occupancy, thus resulting in narrow peaks. Fig. 10 shows that two of these transitions can be observed even at room temperature in absorption spectra. Interestingly, the intensity of these spin-forbidden transitions is highly sensitive to the crystal dimensionality and the exchange interaction pathways. In 0D K_3MnF_6 where $[MnF_6]^{3-}$ units share no common ligands (and therefore lack Mn-F-Mn superexchange pathway) these peaks are not observed, while they exhibit maximum intensity in 2D compounds (i.e., $NaMnF_4$) [80,86].

Single-crystal studies on 1D $Tl_2MnF_5{\cdot}H_2O$ by polarized optical absorption allowed us for the measurement of spin–flip peak absorption along the chain (i.e., along the long Mn-F bond) and perpendicular to it (isotropic spectra along the short Mn-F bonds) [79]. The observation that spin–flip peaks are exclusively polarized along the chain direction, i.e., along the Mn-F-Mn superexchange direction, and their temperature dependence unequivocally indicates that they are activated by the exchange mechanism [79], unlike the broad absorption bands which are activated by odd-parity vibrations.

In 2D A_nMnF_4 layered perovskites, the higher oscillator strength of the spin–flip peaks can be attributed to the presence of multiple in-plane superexchange pathways (four per Mn), enhancing their intensity. Furthermore, the A_n MnF_4 fluorides have attracted significant interest due to their in-plane antiferrodistortive structure. In this arrangement, each F^- ligand acts as a short Mn-F bond for one Mn^{3+} ion and a long Mn-F bond for its in-plane nearest neighbor (Fig. 11). In this situation, the Mn-F-Mn tilt angle, when close to 180°, favors ferromagnetic superexchange within the layer, as evidenced by the occurrence of ferromagnetism below $T_C = 19$ K in $CsMnF_4$ [78,86–89]. A comprehensive review on the magnetic properties of Mn^{3+} fluorides can be found elsewhere [78].

Regarding the spin–flip transitions, an important structural correlation has been established. The exchange-induced oscillator strength of spin–flip transitions in the A_nMnF_4 series exhibits a strong dependence on the tilting angle of $[MnF_6]^{3-}$ connecting octahedra, which directly reflects the strength of the exchange interaction [78,86]. Moreover, the integrated spin–flip peak intensity shows a linear relationship with $\cos^2\varphi$, mirroring the trend observed in exchange interaction determined through magnetic measurements. This correlation is particularly significant as it allows for the extraction of structural information related to the tilting of the octahedra under high pressure.

Fig. 12 illustrates the evolution of the $NaMnF_4$ absorption spectrum under varying pressures. The spin–flip peak intensity exhibits a clear decrease with increasing pressure. This observation suggests that pressure induces a decrease in the tilting angle of MnF_6^{3-} octahedra. A decrease in tilting angle leads to a weaker superexchange interaction, consequently diminishing the intensity of the spin–flip peak. This finding aligns well with the structural trends observed across the A_nMnF_4 series. A reduction in the unit cell volume results in larger tilting and a concomitant weakening of spin–flip peak intensity [86,89].

It is important to note that the d-orbital splitting associated with the broad bands undergoes only minor change under pressure. This observation indicates that the JT distortion remains stable under pressure. Therefore, the primary structural modifications under pressure are associated with tilts of the $[MnF_6]^{3-}$ units.

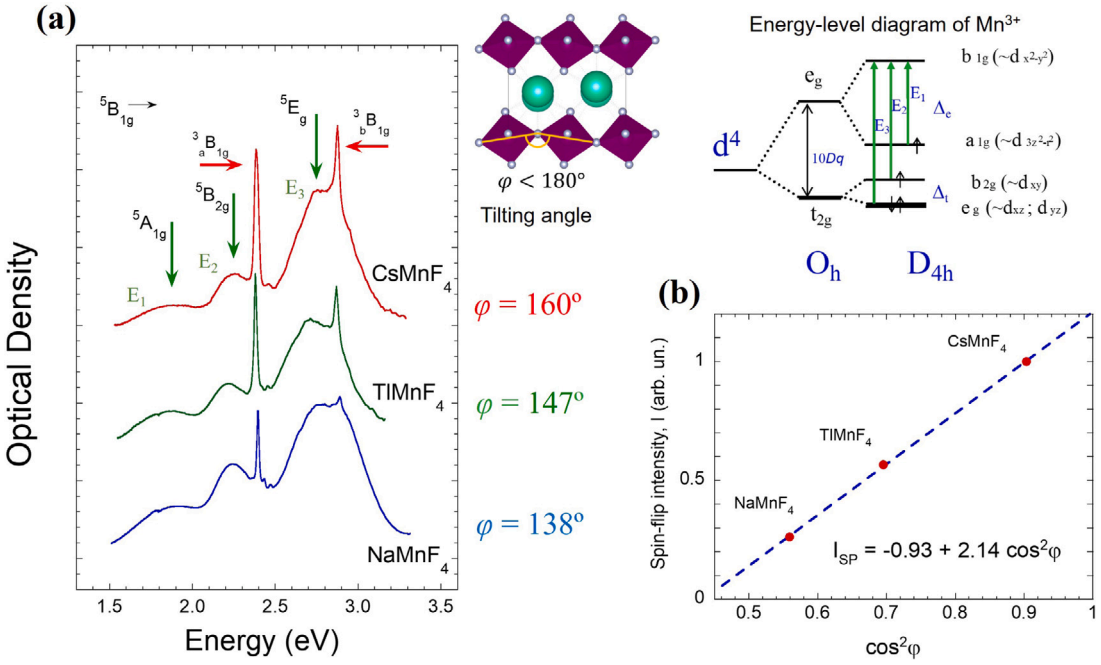

Fig. 11. **(a)** Optical absorption spectra of $NaMnF_4$, $TlMnF_4$, and $CsMnF_4$ single crystals. Mn-F distances R_{ax} and R_{eq} are 2.15, 1.82 Å for $TlMnF_4$, and 2.17, 1.84 Å for $NaMnF_4$ and $CsMnF_4$. The Mn-F-Mn bond angle is indicated on the right [84]. The three spin-allowed crystal-field transitions, E_1, E_2, and E_3, and the spin–flip peaks, E_{SP1} and E_{SP2}, are indicated by vertical green and horizontal red arrows, respectively. **(b)** The spin–flip integrated peak intensity decreases with the tilting angle, φ. Its variation is linear with $\cos^2\varphi$, showing the exchange-induced electric-dipole mechanism of the spin–flip transitions [77,81,85]. The errors are 0.05 and 0.005 for the relative intensity and $\cos^2\varphi$, respectively.

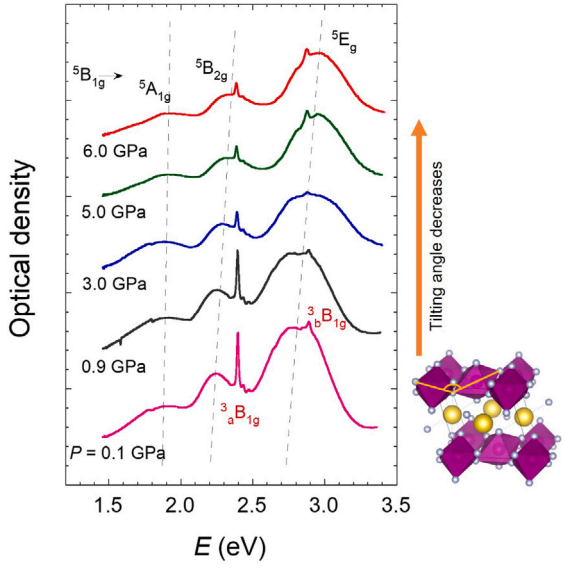

Fig. 12. Variation of the optical absorption spectrum of single crystal of $NaMnF_4$ with pressure in the 0–6 GPa range at room temperature (upstroke). Broken lines illustrate the pressure-induced shift for the three broadbands. Note the spin–flip transition oscillator strengths decrease with pressure, while the absorbance of the three broad bands reflecting the low symmetry Jahn–Teller D_{4h} splitting varies slightly with pressure. This variation is interpreted in terms of pressure-induced MnF_6 tilting, decreasing the in-plane Mn-F-Mn exchange interaction.

3. Heteronuclear and mixed transition-metal/rare-earth systems

3.1. Mn^{2+}–Yb^{3+}

A pioneer and paradigmatic example of a highly efficient Tanabe mechanism in a hybrid transition metal/lanthanide material comes from Cr^{3+}-doped $EuAlO_3$ [13]. In this compound, cooperative absorption and emission transitions overshadow the usual R-lines of Cr^{3+}, which correspond to $^4A_2 \leftrightarrow {}^2E$. While these standard R-line transitions are relatively weak, the sidebands associated with simultaneous excitation of a neighboring Eu^{3+} ion from $^7F_0$ to $^7F_1$ are markedly stronger. Consequently, the Tanabe mechanism induces a large transition dipole moment connecting the $^7F_1$ excited state of Eu^{3+} and the ^2E excited state of Cr^{3+} within the same ion pair. Building on this mechanism, ref. [90] showed how the Tanabe mechanism accounts for the upconversion processes in Yb^{3+}-doped $CsMnCl_3$ and $RbMnCl_3$.

Photon upconversion (UC) describes a process in which infrared radiation is converted into shorter-wavelength ultraviolet or visible light [91]. In the past twenty years, interest in UC has grown because of its relevance to bioimaging [92], display technologies, laser materials, and the potential to boost the performance of bifacial solar cells [93–95].

A material exhibiting photon UC must feature at least two metastable excited states. Lanthanide ions readily provide these states because their shielded *f*-electron configuration weakens electron–phonon coupling. By contrast, transition-metal ions typically undergo strong multiphonon relaxation, making multiple metastable levels comparatively rare [96]. However, when transition-metal ions are combined with lanthanide ions, new mechanisms for upconversion can emerge. In co-doped crystals such as YAG:Nd^{3+},Cr^{3+}, the transition metal ion can serve as a sensitizer, channeling excitation energy into the lanthanide activator [97]. This synergy enables broader tuning of UC luminescence by manipulating both energy resonance conditions and the energies of the emitting states.

3.1.1. *Upconversion mechanism based on exchange interactions*

Among the most significant mechanisms for photon UC are ground-state absorption/excited-state absorption (GSA/ESA), energy-transfer upconversion (GSA/ETU), cooperative luminescence, cooperative sensitization, and photon avalanche processes [91,98]. Additionally, Valiente et al. [90] suggested that exchange interactions between Yb^{3+} and adjacent Mn^{2+} ions can drive an alternative route for UC.

Fig. 13 provides an overview of known UC mechanisms [96]:

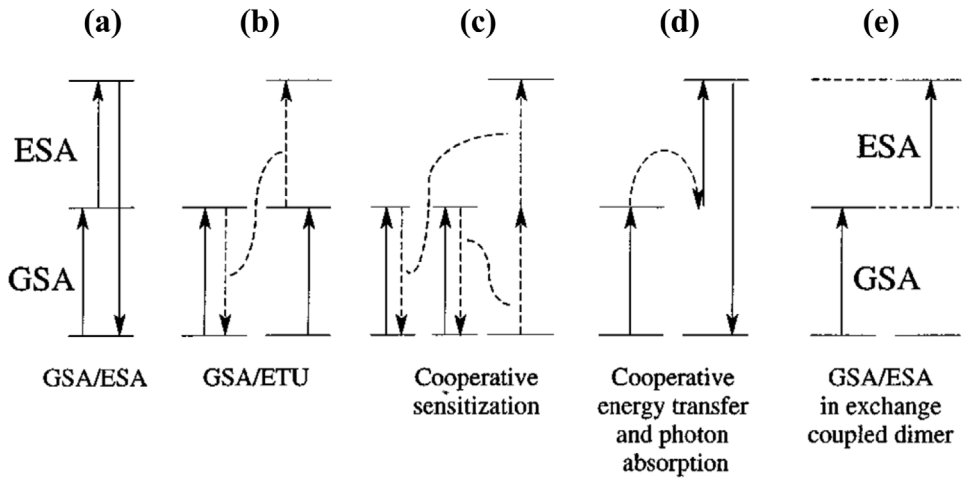

Fig. 13. Schematic depiction of photon upconversion (UC) systems. GSA refers to ground-state absorption, while ESA signifies excited-state absorption. The solid arrow lines denote radiative transitions, while the dotted lines indicate nonradiative processes. Reprinted from Valiente et al. [96]. Copyright (2001), with permission from Elsevier.

- (Fig. 13a) Ground-state absorption/excited-state absorption (GSA/ESA), sometimes called two-step absorption, involves a single ion absorbing a first photon from the ground state and a second photon that raises it to a higher-lying excited state. Because both absorption processes happen during the laser pulse, the UC emission appears just after the pulse is applied.
- (Fig. 13b) Energy-transfer upconversion (GSA/ETU) [91] proceeds when two ions at an intermediate energy level undergo a non-radiative energy transfer between interacting ions. One ion returns to the ground state, while the other is pushed up to a higher excited level. Since this energy transfer does not emit a photon, it can occur after the laser pulse ends, giving rise to a delayed increase in the UC emission.
- (Fig. 13c) Cooperative sensitization requires two excited donor ions to deliver their energy in tandem to an acceptor ion, which otherwise has no level close to the donor excited state [98]. This three-ion mechanism can be significant if donor ions form pairs or if the donor excitation migrates between ions. Like GSA/ETU, it exhibits a slower temporal evolution due to the required energy-transfer step.
- (Fig. 13d) Cooperative energy transfer plus photon absorption involves an excited donor transferring energy to an acceptor that simultaneously absorbs an additional photon [99]. The UC signal from this process arises immediately following the laser pulse.
- (Fig. 13e) Exchange interaction route was suggested by Valiente et al. [90] for systems with Yb^{3+} adjacent to Mn^{2+}, where a GSA/ESA due to direct exchange interaction in the Mn^{2+}–Yb^{3+} pair is responsible for the UC process.

Valiente et al. [96] detailed a GSA/ESA (ground-state absorption /excited-state absorption) scheme for UC. While this process typically involves only a single ion, in their investigation, both Yb^{3+} and Mn^{2+} participate. The relevant intermediate level corresponds to the $^2F_{5/2}$ state of Yb^{3+}, whereas Mn^{2+} emits from its $^4T_1$ level. Because Mn^{2+} lacks an excited state near 10,000 cm^{-1}, the excited Yb^{3+} must itself drive the UC mechanism, necessitating a reinterpretation of standard approaches (Figs. 13a–13d).

Fig. 14a shows the 10 K upconversion emission of $CsMnCl_3$:Yb^{3+} and $RbMnCl_3$:Yb^{3+} under Yb^{3+} excitation. Although Yb^{3+} commonly serves as a sensitizer for various rare-earth ions such as Tm^{3+}, Er^{3+}, Ho^{3+}, and Pr^{3+} [91,100,101], the absence of a suitable Mn^{2+} state around 10,000 cm^{-1} makes the Yb^{3+} role in these chloride hosts uniquely direct. A similar effect can appear in co-doped systems containing Yb^{3+} and Tb^{3+} (CaF_2, SrF_2, YF_3), which exhibit visible Tb^{3+} emission upon Yb^{3+} excitation below 1 μm; however, in this case, cooperative sensitization is usually the observed mechanism [100].

Valiente et al. [96] primarily assessed two possible explanations for the upconversion findings: (i) a process in which two excited Yb^{3+} ions simultaneously hand over energy to a single Mn^{2+} ion [100], and (ii) a combined photon absorption plus Yb^{3+} → Mn^{2+} energy transfer mediated by multipole–multipole interactions [99]. However, they dismissed the first mechanism based on the transient behavior following a short excitation pulse—no delayed rise was observed (Fig. 14b), which argues against a non-instantaneous energy-transfer step. They also ruled out the multipole–multipole model [99] because of the exceptionally high efficiency and clear site selectivity seen in $CsMnCl_3$:Yb^{3+} and $RbMnCl_3$:Yb^{3+}.

All these observations pointed to an exchange interaction mechanism. To interpret this efficiency, a simplified dimer model of Mn^{2+}–Yb^{3+} was proposed [96]. Though it omitted many nuances of the real material, it correctly includes the dominant nearest-neighbor interactions in an insulating magnet. Thus, in this framework, nearest-neighbor Mn^{2+}–Yb^{3+} pairs serve as the fundamental chromophoric units responsible for the UC process.

Fig. 15 presents the Mn^{2+}–Yb^{3+} dimer model, outlining its energy states. The ground state is identified as $|^2F_{7/2},^6A_1\rangle$, while the intermediate near-infrared (NIR) excited state is referred to as $|^2F_{5/2},^6A_1\rangle$. Higher excited states include $|^2F_{7/2},^4T_1\rangle$ and $|^2F_{7/2},^4T_2\rangle$.

The transition from the ground state to the intermediate state, known as the ground-state absorption (GSA) step, benefits from exchange interactions, which enhance its efficiency compared to that of an isolated Yb^{3+} ion. Furthermore, the excited-state absorption (ESA) transitions, such as those from $|^2F_{5/2},^6A_1\rangle$ to $|^2F_{7/2},^4T_1\rangle$ or $|^2F_{7/2},^4T_2\rangle$, are made possible and gain strength through the Tanabe exchange mechanism. Although the intermediate state is predominantly localized on the Yb^{3+} ion, there is some mixing of wavefunctions. Similarly, the emitting state is mainly localized on the Mn^{2+} ion but is not exclusively [96].

3.1.2. Influence of bridging geometry of the superexchange pathway on upconversion efficiency

Exchange interactions between ions in insulating materials are influenced not only by the distance separating the ions but also by the bridging geometry that connects them. This insight led to a systematic investigation of Yb^{3+}-doped Mn^{2+} halides, examining specific bridging geometries between Yb^{3+} and Mn^{2+} ions. Substitution of Mn^{2+} by Yb^{3+} occurs in all studied halides and requires charge compensation. The bridging geometries explored include corner-sharing, edge-sharing, and face-sharing configurations [23].

Among the studied systems, $RbMnCl_3$:Yb^{3+} [96] features corner-sharing and face-sharing geometries, while $CsMnCl_3$:Yb^{3+} [102] and

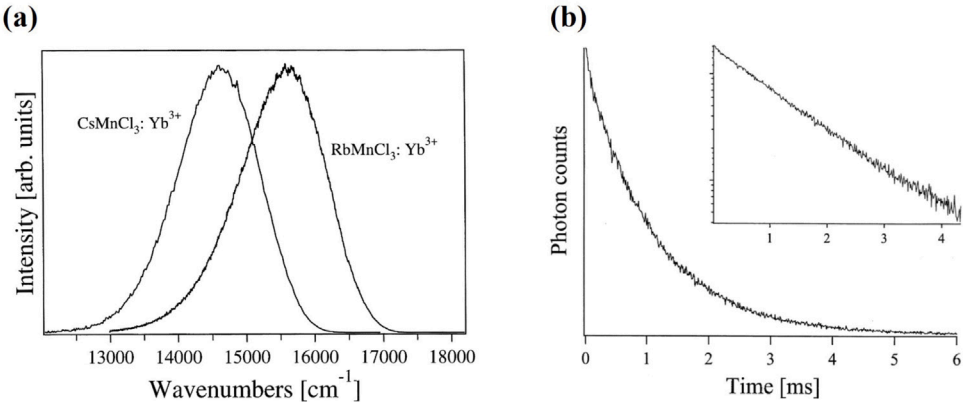

Fig. 14. **(a)** 10 K upconversion luminescence spectra of $CsMnCl_3$:Yb^{3+} and $RbMnCl_3$:Yb^{3+} excited at 10,680 cm^{-1} and 10,688 cm^{-1} ($^2F_{7/2} \rightarrow {}^2F_{5/2}$ absorption from Yb^{3+}), respectively. This represents the first observation of Mn^{2+} upconversion emission, driven by exchange coupling. **(b)** Time evolution at 10 K of the upconverted luminescence intensity of $RbMnCl_3$:Yb^{3+} (observed at 15,750 cm^{-1}) after a 10 ns pulsed excitation at 10,688 cm^{-1}. The inset shows the same data in a semilog representation. The lack of a rise contribution at short times in the transient signal suggests the absence of an energy transfer step. Reprinted from Valiente et al. [90]. Copyright (2000), with permission from Elsevier.

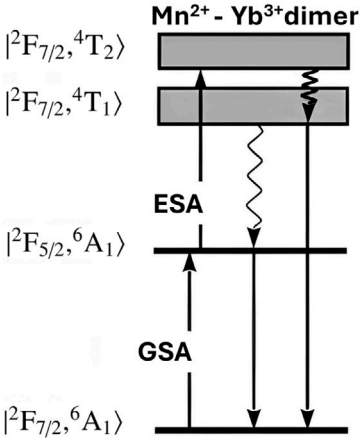

Fig. 15. Schematic upconversion mechanism in a Mn^{2+}–Yb^{3+} dimer. Solid arrows represent the radiative processes of GSA, ESA, and luminescence, whereas the wavy arrow denotes a multiphonon relaxation process. The states are designated using dimer notation. Reprinted from Gerner et al. [23]. Copyright (2004), with permission from John Wiley & Sons.

Rb_2MnCl_4:Yb^{3+} [103] involve corner-sharing connections. Face-sharing geometries are observed in $RbMnBr_3$:Yb^{3+} and $CsMnBr_3$:Yb^{3+} [104]. Additionally, $MnCl_2$:Yb^{3+} and $MnBr_2$:Yb^{3+} were the first examples of edge-sharing geometries to be investigated [23]. Fig. 16 shows some of these structures. It had been established that UC luminescence in these materials was only observable at low temperatures [23,105].

Once the emission spectra have been corrected for the instrumental response at different wavelengths according to the Ejder procedure [106], they can be expressed as photon flux (photons/s). The integrated intensity of the different spectral bands allows for determination of UC efficiency. By comparing how many visible (VIS) photons emitted corresponding to the $|^2F_{7/2}, {}^4T_{1g}\rangle$ transition to the number of near-infrared (NIR) photons emitted from the $|^2F_{5/2}, {}^6A_{1g}\rangle$ state, the UC efficiency can be quantified, assuming that non-radiative relaxation is negligible due to the large energy gap of Mn^{2+} and Yb^{3+}. The UC efficiency is defined as the number of visible emitted photons (VIS_{em}) to the total number of IR absorbed photons (NIR_{abs}):

$$\eta_{UC} = \frac{VIS_{em}}{NIR_{abs}} \tag{14}$$

and the number of NIR absorbed photons can be approximated by

$$NIR_{abs} \cong NIR_{em} + 2 \times VIS_{em} \tag{15}$$

where the factor 2 accounts for the two NIR photons required to generate a single VIS photon, leading to:

$$\eta_{UC} \cong \frac{VIS_{em}}{NIR_{em} + 2 \times VIS_{em}} \tag{16}$$

This approach has been applied to Mn^{2+}–Yb^{3+} systems at temperatures below 100 K.

Based on Eq. (16), the theoretical maximum for η_{UC} is 0.5 (50%), meaning that in the ideal case, every absorbed NIR photon is turned into a VIS photon. In Rb_2MnCl_4:Yb^{3+} at 35 K, 56% of the absorbed NIR photons become VIS photons under the specified excitation conditions [23,103] —an impressively high rate for upconversion. Because UC processes are inherently nonlinear, these efficiencies depend on the specific experimental setup [107]. Moreover, data collected by Gerner et al. [23] highlight the pivotal role of how Yb^{3+} and Mn^{2+} octahedra link together. Moving from corner-sharing (Rb_2MnCl_4:Yb^{3+}) through edge-sharing ($MnCl_2$:Yb^{3+} or $MnBr_2$:Yb^{3+}) to face-sharing ($CsMnBr_3$:Yb^{3+}) reduces the UC efficiency drastically, from 28% down to 0.05% (Fig. 16). This stresses the importance of the bridging geometry in dictating upconversion performance.

In Fig. 17a, the key Mn^{2+}–Yb^{3+} dimer structures are shown with their corresponding nearest-neighbor separations. These Mn–Cl–Yb distances contract from roughly 5.05 Å under corner-sharing coordination down to 3.71 Å for edge-sharing and 3.26 Å for face-sharing [23]. For $MnCl_2$:Yb^{3+} and $MnBr_2$:Yb^{3+}, only edge-sharing configurations are possible, and the data collected [23] reveal that the UC efficiencies in these systems differ by a factor of three — substantially less than the large variations among the distinct bridging geometries. This observation indicates that the type of halide ion does not fundamentally govern the UC performance.

Furthermore, the overall UC efficiency decreases with decreasing Mn^{2+}–Yb^{3+} spacing, making it unlikely that electrical multipole–multipole interactions control the upconversion process. Instead, the strong dependence on geometry points to superexchange interactions as the main driving mechanism for UC in these systems.

In Mn^{2+}–Yb^{3+} pair, Yb^{3+} contributes one unpaired electron while Mn^{2+} carries five. This setup leads to five exchange terms, Eqs. (8) and (10), whose magnitudes depend on the ligand bridging geometry that connects the two metal ions. In the particular case of a corner-sharing arrangement at $\varphi = 180°$ (Fig. 17b), high UC efficiencies can be understood by the strong orbital overlaps that come into play [23]. One key pathway involves the Yb^{3+} $f(z^3)$ orbital, which is assumed to be oriented toward the intervening ligand p_z orbital, thus transferring some spin density onto the bridging ligand. From there, spin density interacts with the singly occupied Mn^{2+} 3d orbitals, the strongest contribution being the $J_{f(z^3)d(z^2)}$ exchange. This interaction is antiferromagnetic and

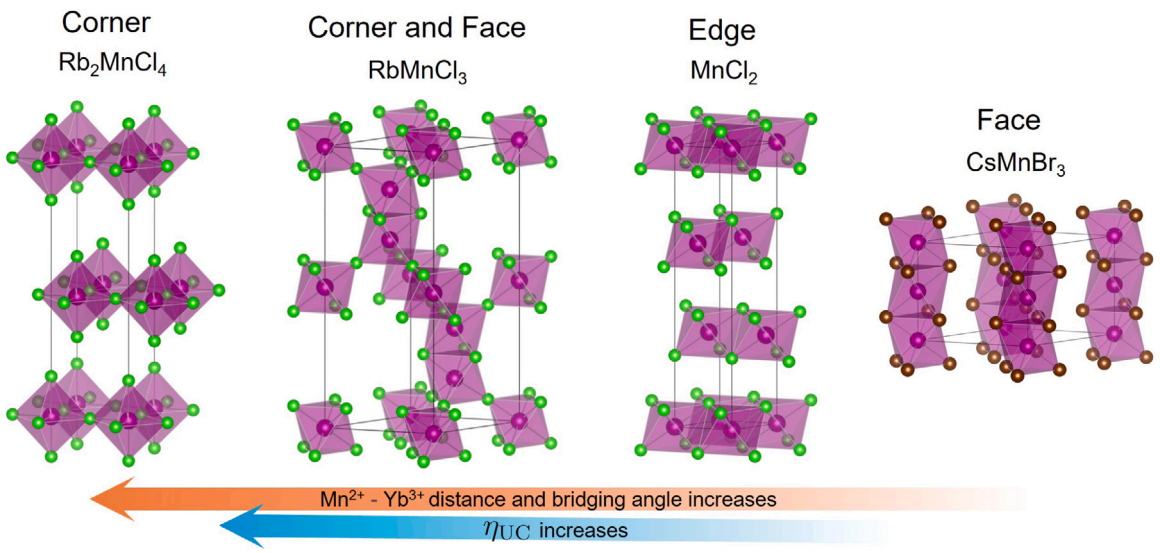

Fig. 16. Examples of different bridging geometries (i.e. super-exchange pathways) in the various pure Mn-based host lattices that have been studied by introducing Yb^{3+} ions. Rb and Cs atoms have been omitted.

gains strength from multiple overlap channels, making it a main factor in the overall exchange-induced optical intensity, Eq. (10). For angles smaller than 180°, these orbital overlaps shrink, and the associated integrals become weaker, which can account qualitatively for the drop in UC efficiency under non-linear bridging [23]. Yet, although this orbital model offers a helpful conceptual framework, it does not precisely match every quantitative detail. Separately, Atanasov et al. [43] proposed a calculation strategy for the necessary transfer integrals and J parameters in rare-earth/transition-metal dimers, showing that, at certain geometries, other exchange pathways might also be relevant.

Therefore, systematic investigations of Mn^{2+}–Yb^{3+} halides have revealed that the upconversion efficiency was governed primarily by the bridging angle (Yb^{3+}–L–Mn^{2+}, where L = Cl or Br). A suitable geometry enabling robust exchange interactions has a greater impact than either the metal–metal spacing or the nature of the bridging halogen. In Rb_2MnCl_4:Yb^{3+}, for instance, such exchange pathways drive a remarkably efficient cooperative UC process at low temperatures.

Unfortunately, all Yb^{3+}-doped Mn^{2+} halides tabulated by Gerner et al. [23] lose their UC luminescence above 150 K. This intrinsic quenching of pure Mn^{2+} compounds arises partly because "killer traps" (e.g., Mn^{3+}) sequester the excitation at elevated temperatures, and partly because a nonradiative decay route depletes the $^4T_1$ level, as indicated by the light curly arrow in Fig. 15. This latter mechanism seems to be even more important in Mn^{2+}–Yb^{3+} systems and is thus not easily bypassed through new material design. As a result, none of the compounds depicted in Fig. 16 are viable upconversion phosphors at room temperature [108].

3.1.3. *Upconversion emission of Mn^{2+}–Yb^{3+} systems at room temperature*

A more promising strategy for high-temperature applications places Mn^{2+} in doubly doped Mn^{2+} and Yb^{3+} lattice with available tetrahedral coordination. Researchers have observed room-temperature Mn^{2+}-based UC in Yb^{3+}/Mn^{2+} co-doped Zn_2SiO_4 [108], $CaZnF_4$ and $SrZnCl_4$ [109], and $LaMgAl_{11}O_{19}$:Mn^{2+},Yb^{3+} [105,110].

Zn_2SiO_4:Yb^{3+},Mn^{2+} represents the first Mn^{2+}–Yb^{3+} UC material shown to produce visible Mn^{2+} luminescence at room temperature, making it readily observable to the human eye [108]. One goal of developing such systems is to enlarge the separation between the $|^2F_{7/2}, {}^4T_1\rangle$ and $|^2F_{5/2}, {}^6A_1\rangle$ transitions, thereby minimizing any associated losses. This motivates the use of Yb^{3+} in combination with Mn^{2+} in a tetrahedral environment rather than an octahedral one. In Zn_2SiO_4:Yb^{3+},Mn^{2+}, the Mn^{2+}–Yb^{3+} dimer model remains a good conceptual tool, and the relevant energy diagram and excitation sequence are illustrated in Fig. 18.

Fig. 18a provides a schematic comparison of the $^4T_1$ and $^4T_2$ excited-state energy levels for Mn^{2+} in octahedral (O_h) coordination (as in $MnCl_2$:Yb^{3+}) versus tetrahedral (T_d) coordination (as in Zn_2SiO_4:Yb^{3+},Mn^{2+}). Notably, shifting Mn^{2+} from an O_h site to a T_d site moves its emission band from red/orange toward green (Fig. 18b), which presents a practical advantage in certain UC applications.

Fig. 19a shows the 12 K excitation spectrum for $MnCl_2$:0.1% Yb^{3+}, focusing on the Yb^{3+} $^2F_{5/2} \rightarrow {}^2F_{7/2}$ emission. Three distinct Yb^{3+} $^2F_{7/2} \rightarrow {}^2F_{5/2}$ peaks appear, the first two as sharp lines and the third as a broader band. Meanwhile, the 12 K absorption spectrum of $MnCl_2$:0.1% Yb^{3+} in Fig. 19b reveals Mn^{2+} $^6A_{1g} \rightarrow {}^4T_{1g}$, $^4T_{2g}$, and $^4A_{1g}/{}^4E_g$ transitions [108].

Figs. 19c and 19d focus on Zn_2SiO_4:6% Yb^{3+},8% Mn^{2+}. In Fig. 19c, the 12 K excitation spectrum displays a structured band corresponding to Yb^{3+} $^2F_{7/2} \rightarrow {}^2F_{5/2}$. At room temperature (Fig. 19d), Mn^{2+} $^4T_1 \rightarrow {}^6A_1$ emission is monitored with excitation peaks corresponding to Mn^{2+} $^6A_1 \rightarrow {}^4T_1$, $^4T_2$, and $^4A_1/{}^4E$ transitions [108].

Comparing Mn^{2+} absorption in $MnCl_2$:Yb^{3+} (Fig. 19b) and Zn_2SiO_4:Yb^{3+},Mn^{2+} (Figs. 19c,d) shows that the $^4T_1$ and $^4T_2$ levels shift to higher energies by about 2000 and 800 cm^{-1}, respectively, in the silicate host due to the lower crystal field $10Dq$ attained in tetrahedral coordination. In contrast, the Yb^{3+} transition energies remain nearly unchanged across these environments — differing by only ~10 cm^{-1}. For $MnCl_2$:Yb^{3+}, the $^2F_{5/2}$ level splits into two clear lines in an octahedral field, whereas Zn_2SiO_4:Yb^{3+},Mn^{2+} exhibits broader peaks, inhomogeneous Yb^{3+} features, pointing to multiple Yb^{3+} sites.

Fig. 20, presents 12 K emission spectra under near-infrared (NIR) excitation for two different Mn^{2+}–Yb^{3+} systems [108]. Fig. 20a shows the $MnCl_2$:0.1% Yb^{3+} emission excited at 10,765 cm^{-1}, yielding a sharp Yb^{3+} NIR emission feature near 10,000 cm^{-1} along with a broad red UC band around 15,240 cm^{-1}, corresponding to the Mn^{2+} $^4T_{1g} \rightarrow {}^6A_{1g}$ transition in an octahedral environment. By contrast, Fig. 20b depicts Zn_2SiO_4:6% Yb^{3+},8% Mn^{2+} excited at 10,891 cm^{-1}, also producing Yb^{3+} emission at ~10,000 cm^{-1} but featuring a green UC band around 19,000 cm^{-1}, assigned to Mn^{2+} $^4T_1 \rightarrow {}^6A_1$ in tetrahedral coordination. Fig. 20c shows a schematic of the Tanabe–Sugano diagram highlighting the change in emission energy as the Mn^{2+} coordination changes (a tetrahedral coordination produces a lower crystal-field strength).

Quantitatively, at 12 K $MnCl_2$:0.1% Yb^{3+} produces red UC accounting for 2.65% of all emitted photons, whereas in Zn_2SiO_4:6% Yb^{3+},8% Mn^{2+} under similar conditions, the green UC makes up only

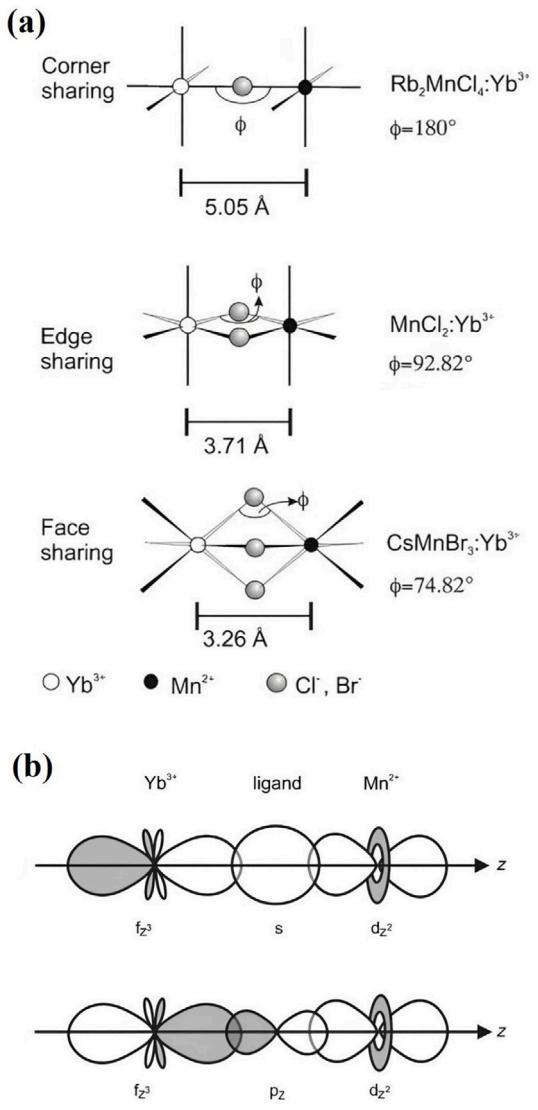

Fig. 17. **(a)** Bridging geometries in Mn^{2+} halide compounds doped with Yb^{3+} between neighboring octahedra. **(b)** The most significant sigma overlaps between completely occupied ligand orbitals and singly occupied metal orbitals are shown schematically for a bridge angle ϕ of 180°. Reprinted from Gerner et al. [23]. Copyright (2004), with permission from John Wiley & Sons.

0.03% [108]. While both systems confirm that NIR pumping of Yb^{3+} leads to visible Mn^{2+} luminescence, the Mn^{2+} emission in Zn_2SiO_4 shifts by about 4,000 cm^{-1} toward the green compared to $MnCl_2$. The presence of Mn^{2+} UC emission in Zn_2SiO_4 implies a close Mn^{2+}–Yb^{3+} interaction within the willemite lattice. However, a factor-of −100 difference in the VIS/NIR photon ratio emerges between the two materials, presumably linked to an unfavorable bridging geometry of the Mn^{2+}–Yb^{3+} pairs in Zn_2SiO_4 relative to $MnCl_2$ [108].

3.2. Mn^{2+}–Cu^{2+}

3.2.1. Band intensity, energy levels, and thermal dependence in Mn^{2+}-Cu^{2+} dimers and trimers

The Tanabe mechanism used to explain the intensity of the $^4A_1/^4E$ Mn^{2+} transitions in Mn^{2+}–Mn^{2+} pair also provides a good framework for understanding Mn^{2+}–Cu^{2+} systems [111–117].

Exchange-coupled clusters — ranging from Mn^{2+}–Cu^{2+} dimers to Cu^{2+}–Mn^{2+}–Cu^{2+} trimers — have been extensively studied in fluoride crystals like $KZnF_3$:Mn^{2+},Cu^{2+} [111,112] and K_2CuF_4:Mn^{2+} [117], as well as in organometallic complexes [113–117]. Insights into the associated exchange interactions typically come from analyzing the fine structure in the $^6A_1 \rightarrow {}^4E$, $^4A_1$ spin–flip transition of Mn^{2+} and monitoring its thermal behavior. By examining these optical features, one can determine exchange constants for both ground and excited states.

Some Mn-F-Cu networks exhibit notably large J values. For instance, K_2CuF_4:Mn^{2+} has $J = 25$ cm^{-1} [117], while $KZnF_3$:Mn^{2+},Cu^{2+} measures $J = 65$ cm^{-1} [111], based on an exchange Hamiltonian, Eq. (3). These coupling strengths surpass by an order of magnitude the antiferromagnetic $J = -3.4$ cm^{-1} reported for $RbMnF_3$ [118] or the ferromagnetic $J = 8.8$ cm^{-1} of K_2CuF_4 [119]. Moreover, when Mn^{2+} is in its $^4A_1$ excited state, the ferromagnetic coupling to Cu^{2+} (J^*) rises by 20%–50% compared to the ground-state value (J) [111,112,117].

Nevertheless, while the exchange mechanism boosts the transition intensities compared to isolated $[MnF_6]^{4-}$ centers, it does not push oscillator strengths beyond $\sim 10^{-4}$–10^{-3}. This is noticeably smaller than the $\sim 3 \times 10^{-2}$ observed for the 25,000 cm^{-1} band in A_2MnCl_4:Cu^{2+} (A: methylammonium ion), underscoring that even strong exchange interactions cannot entirely account for such a high oscillator strength.

Valiente and Rodríguez [120] attributed the stronger absorption features and the appearance of new bands in the optical spectra of $A_2Cd_{1-x}Mn_xCl_4$:Cu^{2+} crystals to Mn^{2+}–Cu^{2+} exchange coupling rather than to isolated $[CuCl_4]^{6-}$ complexes (). Their work sought to clarify how substituting Mn^{2+} into the A_2CdCl_4 host influences the Cu^{2+}-related absorption bands, focusing particularly on temperature-dependent behaviors and charge-transfer (CT) spectra, which themselves depend strongly on the tetragonal distortion around $[CuCl_4]^{6-}$.

Increased Mn^{2+} content enhances the intensity of the Cu^{2+}-associated absorption bands, an effect explained by an exchange interaction between Mn^{2+} and Cu^{2+}. The same interaction yields a broad band near 21,000 cm^{-1} and a more narrowly defined band at 25,000 cm^{-1}, causing the crystal color to shift from pale yellow to deep red as Mn content, x, grows from 0 to 1 in $A_2Cd_{1-x}Mn_xCl_4$:Cu^{2+}. The temperature dependence of these new bands through a spin-dependent transition mechanism operative within Mn^{2+}–Cu^{2+} pairs [120]. Consequently, the two distinct peaks at 21,000 and 25,000 cm^{-1} in A_2MnCl_4:Cu^{2+} are firmly ascribed to exchange-coupled Mn^{2+}–Cu^{2+} units.

Unlike the situation in fluorides, the $^4A_1$-^4E excitation of Mn^{2+} in the Mn^{2+}–Cl^-–Cu^{2+} arrangement here resonates with the 25,000 cm^{-1} $Cl^-_{(eq)} \rightarrow Cu^{2+}$ CT transition. This resonance implies that Mn^{2+} transitions can display higher oscillator strengths than those observed in corresponding Mn^{2+}–F^-–Cu^{2+} compounds, especially if the main route for enhancing Mn^{2+} transition intensity involves mixing with CT states via configuration interaction in the exchange-coupled lattice. Consequently, the two strong absorption features detected in A_2MnCl_4:Cu^{2+} and $A_2Cd_{0.7}Mn_{0.3}Cl_4$:Cu^{2+} arise from electronic transitions in Mn^{2+}–Cu^{2+} pairs, moving from the ground state to excited states whose wavefunctions incorporate both the odd-symmetry $Cl^- \rightarrow Cu^{2+}$ CT states of the $[CuCl_6]^{4-}$ complex and the spin–flip excitations of Mn^{2+} [120].

The optical absorption spectra of $A_2Cd_{1-x}Mn_xCl_4$:Cu^{2+} (Fig. 21) can be rationalized by recognizing that Mn^{2+}–Cu^{2+} dimers predominate at $x = 0.3$, whereas Mn^{2+}–Cu^{2+}–Mn^{2+} trimers become the main species when $x = 1$ [120]. Under the assumption of a random replacement of Cd by Mn, $A_2Cd_{0.7}Mn_{0.3}Cl_4$:Cu^{2+} contains about 19% isolated $[CuCl_6]^{4-}$ monomers, 66% Mn–Cl–Cu dimers, and 15% Mn–Cl–Cu–Cl–Mn trimers [120]. Only trimers with 180° bond angles are considered in this analysis.

Fig. 21 reveals two absorption bands at 25,000 and 21,000 cm^{-1}, each linked to distinct Mn^{2+}–Cu^{2+} exchange pathways [120]. Their relative intensities shift with the Mn concentration, consistent with this interpretation. The strong 25,000 cm^{-1} band at $x = 0.3$ indicates a greater prevalence of Mn^{2+}–Cu^{2+} pairs bridged via the equatorial Cu–Cl bond, rather than the axial one. Moving from $x = 0.3$ to $x = 1$ alters

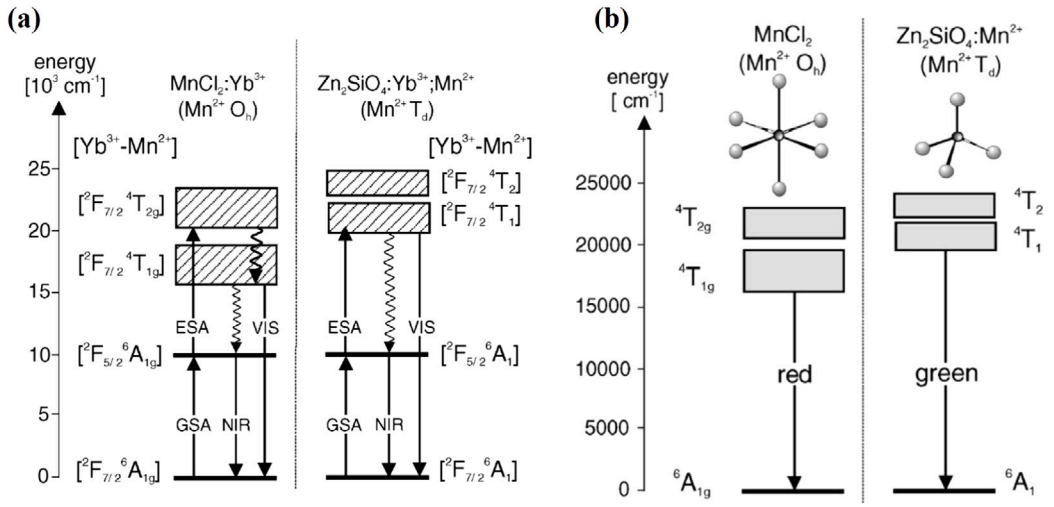

Fig. 18. **(a)** Mn^{2+}–Yb^{3+} dimer states and transitions are shown schematically for the octahedral case (O_h) of $MnCl_2$:Yb^{3+} and the tetrahedral (T_d) example of Zn_2SiO_4:Yb^{3+},Mn^{2+}. Radiative and nonradiative processes are denoted by straight and curly arrows, respectively. **(b)** Energy level diagrams for the first two excited states of octahedral ($MnCl_2$) and tetrahedral (Zn_2SiO_4:Mn^{2+}) Mn^{2+} coordination, highlighting the variation in the emission band. Reprinted from Gerner et al. [108]. Copyright (2004), with permission from Elsevier.

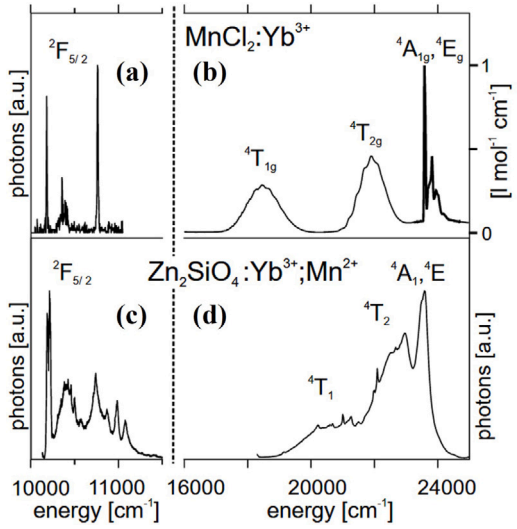

Fig. 19. **(a)** 12 K excitation spectra of Yb^{3+}, monitoring the $^2F_{5/2}$ emission at 9,820 cm^{-1}. **(b)** 6 K absorption spectra of $MnCl_2$:Yb^{3+}. **(c)** 12 K excitation spectra of Yb^{3+} for the $^2F_{5/2}$ emission at 10,100 cm^{-1}. **(d)** 300 K excitation spectra of Mn^{2+} monitoring the Mn^{2+} emission at 17,390 cm^{-1} in Zn_2SiO_4:Yb^{3+},Mn^{2+}. Reprinted from Gerner et al. [108]. Copyright (2004), with permission from Elsevier.

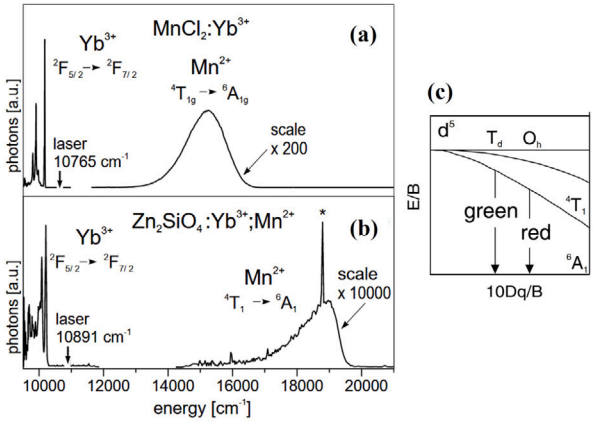

Fig. 20. **(a)** Emission spectra of $MnCl_2$:Yb^{3+} under laser stimulation at 10,765 cm^{-1} at 12 K. **(b)** 12 K emission spectra of Zn_2SiO_4:Yb^{3+},Mn^{2+} during laser excitation at 10,891 cm^{-1}. The asterisk (*) indicates a peak resulting from stray light of the 532 nm pump source. Note the varying scaling factors for VIS emissions. **(c)** Tanabe–Sugano diagram for a d^5 configuration. The arrows depict the transition of Mn^{2+} luminescence from red to green as it shifts from octahedral (O_h) to tetrahedral (T_d) coordination. Reprinted from Gerner et al. [108]. Copyright (2004), with permission from Elsevier.

these intensities, suggesting that more Mn^{2+}–Cu^{2+} pairs form when the crystal is fully substituted, though the total number of pairs remains constant at $x = 1$.

The authors proposed a simplified spin-based framework to interpret the energy levels of Mn^{2+}–Cu^{2+} dimers and Mn^{2+}–Cu^{2+}–Mn^{2+} trimers, illustrated in Fig. 22 [120]. Their model uses the effective exchange Hamiltonian, Eq. (3), capturing the coupling for both the ground (J) and excited (J^*) states. In the dimer, Mn^{2+} has spin $S_{Mn} = 5/2$, and Cu^{2+} has spin 1/2; in trimers, two Mn^{2+} ions can generate S_{Mn} values of 5, 4, 3, 2, 1, or 0 when combined, again paired with Cu^{2+} ($S_{Cu} = 1/2$).

Although this approximate method may shift the energies of individual sublevels, the resulting state labels and the transition selection rules mirror those obtained via a more detailed exchange operator, Eq. (1). Assuming D_{2h} symmetry for the Mn^{2+}–Cu^{2+}–Mn^{2+} trimer [120] matches the crystal structure, the ground state is written as $|^6A_1(a), {}^2A_1, {}^6A_1(b)\rangle$, which corresponds to a combination of A_{1g} and B_{1u} irreps. Meanwhile, the unpaired Cu^{2+} d orbital (primarily $d_{x^2-y^2}$) transforms as a_{1g} in that same symmetry. Coupling three spins (two Mn^{2+} sites plus one Cu^{2+}) results in 11 spin configurations.

Two specific Mn-related excited states, $|^4A_1(a), {}^2A_1, {}^4A_1(b)\rangle$ and $|^6A_1(a), {}^2A_1, {}^4A_1(b)\rangle$, generate excited trimer states labeled $^9B_{1g}$, $^9B_{1u}$, and so on (Fig. 22). These excited states may become degenerate if the exchange interaction between them satisfies:

$$\langle {}^4A_1(a), {}^2A_1, {}^6A_1(b)|\ H_{ex}\ |{}^6A_1(a), {}^2A_1, {}^4A_1(b)\rangle = 0,$$

meaning no splitting arises for states having the same total spin [120].

Although the diagram anticipates two possible transitions for the dimer and 19 for trimers, they cannot be individually observed in practice, so extracting the excited-state exchange J^* directly from absorption data proves difficult. However, measuring how the total oscillator strength $f(T)$ varies with temperature, along with knowledge of each trimer sublevel intensity, can reveal the ground-state exchange constant J.

By examining how $f(T)$ changes with temperature, one can differentiate between dimers and trimers, since each displays a unique thermal

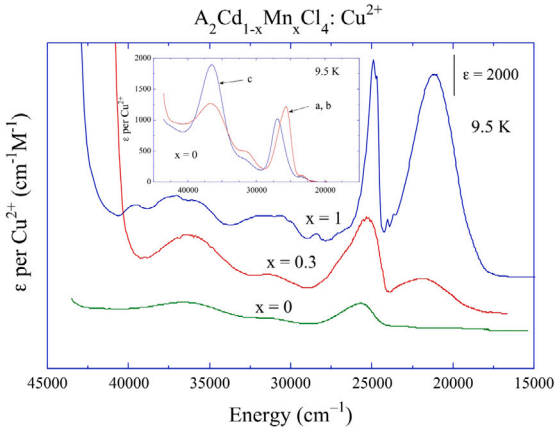

Fig. 21. Polarized optical absorption spectra were recorded at T = 9.5 K for the $A_2Cd_{1-x}Mn_xCl_4$:Cu^{2+} (A =CH_3NH_3) crystal series, with x values of 0, 0.3, and 1. The measurements were polarized along the a and b crystallographic directions. For $x = 0$, the inset displays the corresponding spectra along all three orthorhombic directions, providing a complete view of the optical behavior in these orientations. Copyright (1996), with permission from Elsevier.
Source: Adapted from Valiente and Rodríguez [120].

pattern. For dimers and trimers, the relevant $f(T)$ dependencies are given by [120]:

$$f(T) = \frac{f(0)}{1 + \left(\frac{7}{5}\right)\exp\left(\frac{-3J}{kT}\right)} \tag{17}$$

$$f(T) = 11 \times f(0) \times \frac{\sum_i I_i \exp\left(\frac{-E_i}{kT}\right)}{Z} \tag{18}$$

In the trimer case, the partition function is labeled as

$$Z = \sum_i g_i \exp\left(\frac{-E_i}{kT}\right), \tag{19}$$

and each ground-state sublevel has a normalized intensity I_i, an energy E_i, and a spin degeneracy g_i.

In the case of Mn^{2+}–Cu^{2+} dimers, the oscillator strength $f(T)$ can be determined exactly, since only the $^5A_1$ ground sublevel contributes to the transitions. However, Mn^{2+}–Cu^{2+}–Mn^{2+} trimers introduce multiple sublevels for the ground state, so $f(T)$ hinges on various intensity factors, I_i. These quantities were computed [113] for the $^6A_1 \rightarrow {}^4A_1$ spin–flip transition of Mn^{2+} in trimeric systems. Following the framework of ref. [113], the values of I_i can be obtained from a spin-dependent transition-moment operator $\mathbf{P}^B_{ex}$, Eq. (9), which governs the exchange interaction in Mn^{2+}–Cu^{2+} pairs [4,121].

Experimental measurements of the temperature dependence of the oscillator strength, $f(T)$, for the two prominent absorption bands in A_2MnCl_4:Cu^{2+} ($25,000\,cm^{-1}$ and $21,000\,cm^{-1}$) align well with a trimer model that uses the intensity values computed from an analogous relation [113]. Although the moment operator $\mathbf{P}^B_{ex}$ strictly applies only to spin–flip excitations without any orbital reconfiguration, this agreement implies a comparable spin-dependent mechanism operates in the trimer excitations of A_2MnCl_4:Cu^{2+}.

Notably, a dimer-based approach, Eq. (17), cannot reproduce the observed *f(T)* behavior, confirming that these transitions must be understood in terms of trimers (or larger aggregates). In principle, $x = 1$ yields a Cu^{2+}-centered pentamer (one Cu^{2+} surrounded by four Mn^{2+}), yet the band-intensity data still obey Eq. (18), consistent with trimer-like thermal dependence. The two bands at 25,000 and $21,000\,cm^{-1}$ apparently correspond to Mn^{2+}–Cu^{2+} transitions through equatorial and axial Cu–Cl links of the $[CuCl_6]^{4-}$ Jahn–Teller units, respectively [120].

Fig. 23 illustrates how a least-squares fit to Eq. (18) gives ground-exchange constants J(eq) = 85 cm^{-1} (for the 25,000 cm^{-1} band) and J(ax) = 65 cm^{-1} (for the 21,000 cm^{-1} band). These distinct values of J(eq) and J(ax) reinforce that the two bands spring from separate Mn^{2+}–Cu^{2+} interaction pathways, confirming the present assignment of their origins.

3.3. Mn^{2+}–Ni^{2+}

Exchange effects due to the Mn^{2+}–Ni^{2+} interaction were first observed in $KMn_xNi_{1-x}F_3$ crystals [9,122,123]. Among transition-metal ions, Ni^{2+} is one of the few that exhibits luminescence from two excited states — an exception to Kasha's rule [124], which establishes that any observable luminescence arises solely from the lowest excited state — (Fig. 24a). The existence of at least two metastable states is a fundamental requirement for photon-upconversion processes to occur (see Section 3.1). The first of these excited states acts as a temporary energy reservoir. From that level, population of higher-energy states becomes feasible, leading to emission at shorter wavelengths after excitation at longer wavelengths [125,126]. Fig. 24b [127] illustrates a simplified energy-level diagram for Ni^{2+}, emphasizing the luminescence transitions.

Nonetheless, the overall efficiency of Ni^{2+} upconversion (UC) is limited by low ground-state-absorption (GSA) and excited-state-absorption (ESA) cross sections, especially in chloride matrices. The reason for this limitation is that these transitions are spin forbidden. As it has been shown in the Introduction, exchange interactions between neighboring transition-metal ions in insulating solids can dramatically enhance the intensities of spin-forbidden $d - d$ transitions [5,128]. In Ni^{2+}-doped $RbMnCl_3$, for example, the UC rate is notably higher than in the analogous $CsCdCl_3$:Ni^{2+} [22,129]. Later on, these authors focused on how Mn^{2+}-Ni^{2+} exchange interactions influence Ni^{2+} optical properties and UC luminescence behavior. Their research involved the comparison of two isostructural layered perovskite host lattices for Ni^{2+}, Rb_2CdCl_4 and Rb_2MnCl_4 [130,131]. These layers consist of corner-sharing $[MCl_6]^{4-}$ octahedra, separated by Rb^+ ions, and are slightly compressed along the c-axis, yielding a D_{4h} site symmetry. This structural anisotropy is crucial for studying exchange effects because the exchange interactions occur only within the layers and can be selectively activated or deactivated with polarized light.

In Rb_2MnCl_4:Ni^{2+} specifically, the nearly linear Ni^{2+}-Cl^--Mn^{2+} bridging geometry facilitates strong antiferromagnetic superexchange, significantly impacting the optical-spectroscopic features of Ni^{2+}. When measured perpendicular to the perovskite planes, Ni^{2+} behaves like the standard diamagnetic Ni^{2+}-doped crystal (Rb_2CdCl_4). However, with in-plane (σ) polarized light, i.e., the electric field of light perpendicular to the layer or, in other words, parallel to the Ni^{2+}-Cl^--Mn^{2+} direction, the cross sections for the Ni^{2+} $^3A_{2g} \rightarrow {}^1E_g$ GSA and $^3T_{2g} \rightarrow {}^1T_{2g}$ ESA transitions are boosted by factors of 10 and 6, respectively, compared to π polarization. Consequently, the UC emission intensifies by about a factor of 60 for σ compared to π excitation.

3.3.1. *Exchange enhancement of Mn^{2+}–Ni^{2+} absorption in Ni^{2+}-doped manganese chlorides*

In diamagnetic crystals like Rb_2CdCl_4, spin–orbit coupling to nearby spin-allowed transitions allows Ni^{2+} to circumvent spin-selection rules. Accordingly, the $^3A_{2g} \rightarrow {}^1E_g$ transition of Ni^{2+} in Rb_2CdCl_4 shows an almost polarization-independent oscillator strength [127]. When the same transition is examined in σ-polarized light for Rb_2MnCl_4: 5% Ni^{2+}, the oscillator strength increases an order of magnitude. In contrast, no equivalent gain is observed under π polarization. This polarization behavior was attributed to the role of Mn^{2+}-Ni^{2+} exchange interactions confined to the perovskite layers. This phenomenon bears resemblance to the boost in otherwise spin-forbidden $d - d$ transitions seen in Mn^{2+} systems such as MnF_2 and $RbMnF_3$, originally investigated in detail by Ferguson, Guggenheim, and Tanabe. Whereas Mn^{2+} features one unpaired electron in each d orbital, Ni^{2+} only has its unpaired electron density in the e_g orbitals, implying that Mn^{2+}-Ni^{2+} exchange follows a σ-type coupling, as illustrated in Fig. 25a (scheme I). In

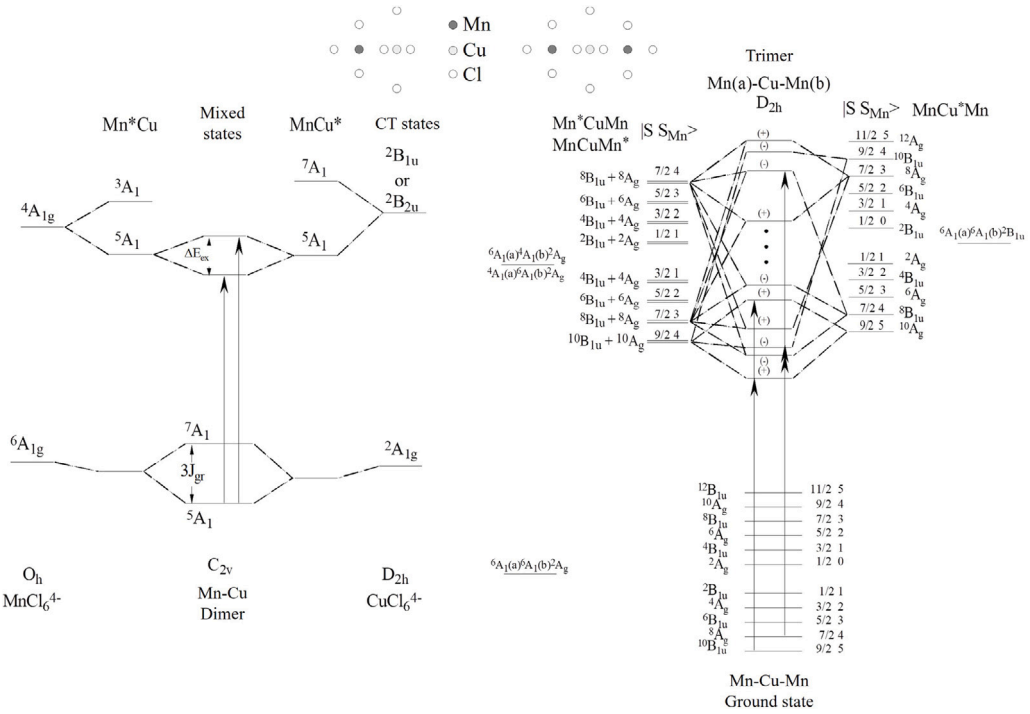

Fig. 22. Schematic energy level diagrams for a Mn^{2+}–Cu^{2+} dimer and a Mn^{2+}–Cu^{2+}–Mn^{2+} trimer. The resonant Cl^- to Cu^{2+} charge transfer states have been incorporated in every instance. Arrows denote the electric dipole transitions permitted by symmetry. In both instances, transitions are polarized along the Mn^{2+}–Cu^{2+} axis. To ensure clarity, exclusively the sublevels and electronic transitions associated with the greatest spin values of the trimer are presented. The (+) and (−) symbols indicate the even and odd parity of the sublevel, respectively. Reprinted from Valiente and Rodríguez [120]. Copyright (1996), with permission from Elsevier.

Rb_2MnCl_4:Ni^{2+}, the Ni^{2+}-Cl^--Mn^{2+} bridge runs in a linear arrangement, establishing a robust superexchange path through Cl^- 3s and $3p_z$ orbitals [27].

Because this variety of exchange interaction arises solely within the perovskite layers, the spin-forbidden $^3A_{2g} \rightarrow {}^1E_g$ transition of Ni^{2+} is enhanced only for σ polarization [127]. In Rb_2MnCl_4: Ni^{2+}, most Ni^{2+} ions have four Mn^{2+} neighbors in the same layer, indicating that an actual spin cluster might be a $Ni^{2+}(Mn^{2+})_4$ pentamer [16,132,133]. Still, the simplified Mn^{2+}-Ni^{2+} pair description was adequate to illustrate the exchange effect and its influence on Ni^{2+} optical spectra. According to the Kanamori–Goodenough rules [26,134], the Ni^{2+}-Cl^--Mn^{2+} superexchange route (Fig. 25a, scheme I) pointed to a dominant antiferromagnetic interaction between Ni^{2+} and Mn^{2+}. In that scenario, the $|Ni^{2+}(^3A_{2g}), Mn^{2+}(^6A_{1g})\rangle$ ground state splits into $S = 3/2$, 5/2, and 7/2 pair spin levels, as sketched in Fig. 25b [9]. The key excited pair state mainly from Ni^{2+}, $|Ni^{2+}(^1E_g), Mn^{2+}(^6A_{1g})\rangle$, holds $S = 5/2$, enabling a formally spin-allowed transition within $S = 5/2$ states (depicted by the arrow in Fig. 25b). Therefore, this pair transition acquires oscillator strength through the Tanabe mechanism, requiring thermal activation since the low-energy spin state corresponds to the $S = 3/2$ according to the antiferromagnetic coupling. The experimental observations by Wenger et al. [127] confirmed this: for 5% Ni^{2+}:Rb_2MnCl_4, the σ-polarized ^1E_g absorption grows by about a factor of two up to 200 K (relative to its value at 15 K), after which it diminishes slightly.

The pronounced enhancement of Ni^{2+} spin–flip transitions is influenced by the geometry of the Ni^{2+}-Cl^--Mn^{2+} connection. As shown in Fig. 26, the 15 K absorption spectra of Ni^{2+} $^3A_{2g} \rightarrow {}^3T_{2g}$, $^3T_{1g}(^3F)$, and ^1E_g in four different Mn^{2+} host crystals are depicted, where the axial and σ polarizations are equivalent in this case, both corresponding to spectra obtained with the electric field of light perpendicular to the layer. Once a Ni^{2+} ion substitutes a Mn^{2+} ion, the Mn^{2+}-Ni^{2+} linkage geometries vary substantially between host lattices. Exchange-related intensity increases in the ^1E_g band occur in Ni^{2+}-doped $RbMnCl_3$ (c) and Rb_2MnCl_4 (d), but not in $CsMnCl_3$ (a) or $MnCl_2$ (b).

A direct comparison with their bridging geometries confirms that this strong intensity enhancement only emerges when the Ni^{2+}-Cl^--Mn^{2+} bond is nearly 180°. This observation aligns with the orbital models of Fig. 25a, where scheme I illustrates a robust σ-type superexchange route that yields strong antiferromagnetic coupling, thereby amplifying spin–flip transitions by the Tanabe mechanism. Such a linear arrangement appears in $RbMnCl_3$: Ni^{2+} and Rb_2MnCl_4: Ni^{2+} [130,135], explaining the marked effect on spin–flip transitions. In contrast, $MnCl_2$: Ni^{2+} and $CsMnCl_3$: Ni^{2+} show edge- or face-sharing octahedra linking Ni^{2+} and Mn^{2+}, consistent with scheme II in Fig. 25a. In that configuration, the magnetic orbitals are orthogonal, eliminating an antiferromagnetic superexchange pathway and thus preventing any Tanabe-mediated enhancement.

3.3.2. Exchange enhancement of luminescence transitions in Mn^{2+}–Ni^{2+} systems

The 15 K emission spectrum of a Rb_2CdCl_4: 5% Ni^{2+} crystal (Fig. 27a) exemplifies the typical Ni^{2+} luminescence features found in diamagnetic halides. As depicted schematically in Fig. 24b, emission arises from $^1T_{2g}$ and extends to all lower-energy levels in the Ni^{2+} manifold. At 15 K, Rb_2MnCl_4: 5% Ni^{2+} (Fig. 27b) shows Ni^{2+} luminescence again [127]; however, no Mn^{2+} emission is observed. Moreover, the relative intensity of the $^1T_{2g} \rightarrow {}^3A_{2g}$ transition and the σ-polarized $^1T_{2g} \rightarrow {}^3T_{2g}$ luminescence in Rb_2MnCl_4: Ni^{2+} is enhanced by roughly a factor of five compared to Rb_2CdCl_4: Ni^{2+} [127]. Notably, this boost is seen most prominently in the electronic-origin region, signifying increased allowed character in the magnetically active host.

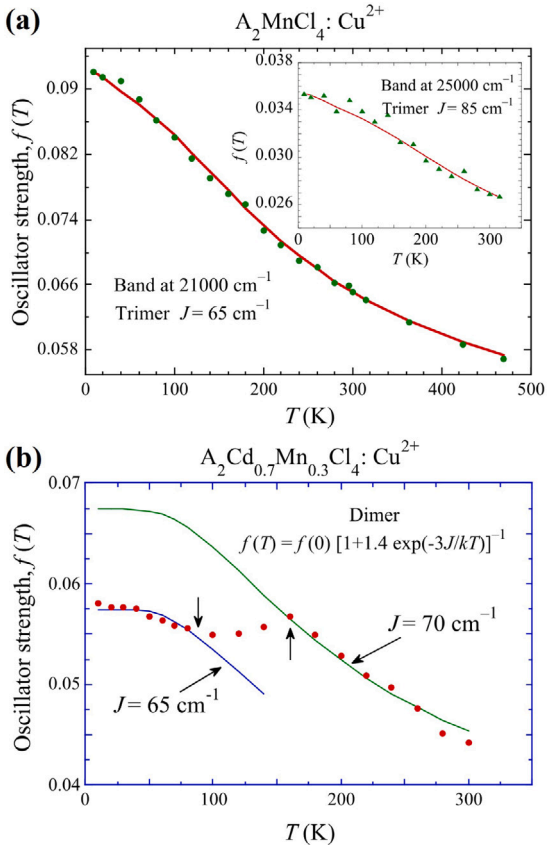

Fig. 23. Temperature dependence of the oscillator strength for bands at 25,000 and 21,000 cm^{-1} (inset) was measured in **(a)** A_2MnCl_4:Cu^{2+} and the two bands in **(b)** $A_2Cd_{0.7}Mn_{0.3}Cl_4$:Cu^{2+} (A = CH_3NH_3). The solid lines depict the least-squares fitting of the experimental $f(T)$ data to Eq. (18) for A_2MnCl_4:Cu^{2+} and to Eq. (17) for $A_2Cd_{0.7}Mn_{0.3}Cl_4$:Cu^{2+}. Copyright (1996), with permission from Elsevier.
Source: Adapted from Valiente and Rodríguez [120].

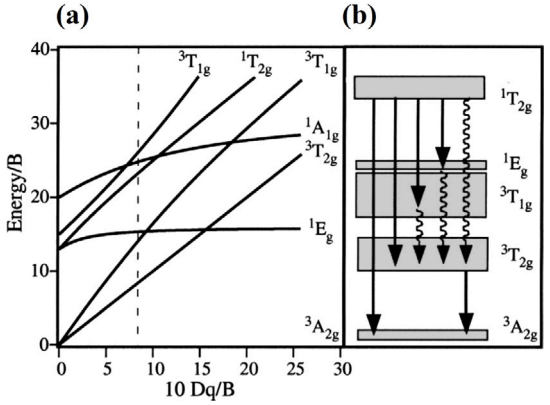

Fig. 24. **(a)** A Tanabe–Sugano plot for Ni^{2+} (d^8) under octahedral coordination. The dashed line indicates the crystal field strength of the Rb_2MCl_4 (M = Mn, Cd) compounds. **(b)** A simplified energy-level scheme for Ni^{2+} with the luminescence transitions (solid arrows) and the nonradiative relaxation through multiphonon processes (wavy arrows). Reprinted with permission from Wenger et al. [127]. Copyright (2001) by the American Physical Society.

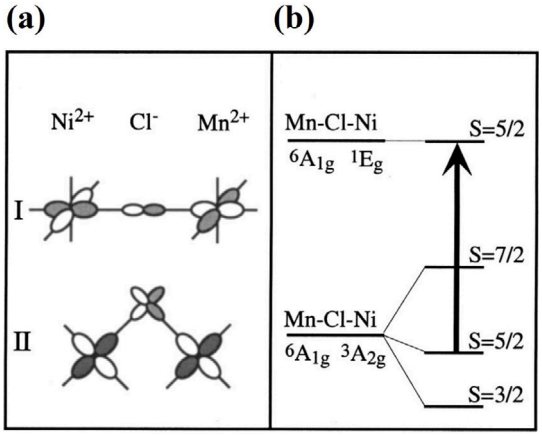

Fig. 25. **(a)** Molecular-orbital sketches that depict the Ni^{2+}-Cl^--Mn^{2+} exchange pathways, forming (I) a 180 ° and (II) a 90 ° configuration. **(b)** Simplified energy levels for a Mn^{2+}-Ni^{2+} pair, highlighting the Ni^{2+} $^3A_{2g}$ → ^1E_g thermally activated transition associated with the spin-allowed transition. Reprinted with permission from Wenger et al. [127]. Copyright (2001) by the American Physical Society.

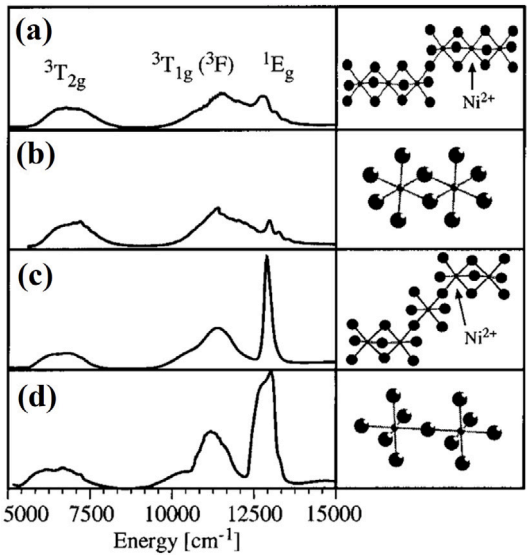

Fig. 26. 15 K axial absorption spectra of **(a)** $CsMnCl_3$: 10% Ni^{2+} (axial), **(b)** $MnCl_2$: 5% Ni^{2+} (axial), **(c)** $RbMnCl_3$: 10% Ni^{2+} (axial), and the σ-polarized **(d)** Rb_2MnCl_4: 5% Ni^{2+}. The featured range covers the Ni^{2+} $^3A_{2g}$ → $^3T_{2g}$, $^3T_{1g}$(^3F), and ^1E_g transitions. Relevant connections between octahedra of each crystal structure are depicted, illustrating how Ni^{2+} and Mn^{2+} are connected in these four systems. Reprinted with permission from Wenger et al. [127]. Copyright (2001) by the American Physical Society.

This intensified $^1T_{2g}$ → $^3T_{2g}$ emission was interpreted according to the Tanabe mechanism, which accounts for exchange-induced enhancements. Since $^3T_{2g}$ and $^1T_{2g}$ originate from the same electronic configuration in the strong-field regime, the $^1T_{2g}$ →$^3T_{2g}$ transition qualifies as a spin–flip event, involving parallel states in the Tanabe–Sugano diagram (see Fig. 3(a)). In contrast, the $^1T_{2g}$ → $^3A_{2g}$ and $^1T_{2g}$ → $^3T_{1g}$(^3F) transitions are not purely spin–flip transitions and are therefore less affected by exchange interactions [127]. This outcome has two important implications. First, the inverse transition, $^3T_{2g}$ → $^1T_{2g}$, becomes relevant to Ni^{2+} UC processes. Second, the augmented probability for the $^1T_{2g}$ → $^3T_{2g}$ emission transition will modify the $^1T_{2g}$ state lifetime [127].

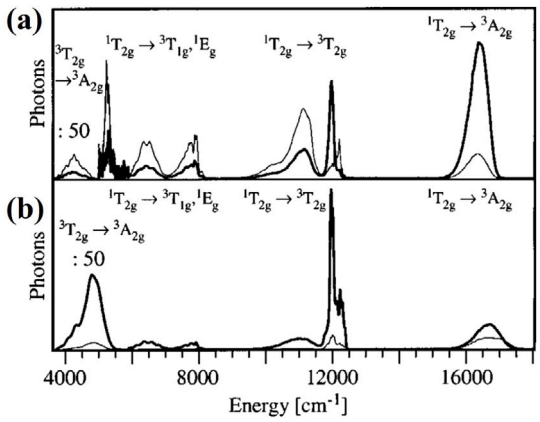

Fig. 27. 15 K polarized luminescence spectra of (a) Rb_2CdCl_4: 5% Ni^{2+} and (b) Rb_2MnCl_4: 5% Ni^{2+}. The thick lines represent the σ-polarized spectra, whereas the thin lines show the π-polarized signals. Note the scale-down applied in every emission spectrum of the $^3T_{2g} \rightarrow {}^3A_{2g}$ transition. Reprinted with permission from Wenger et al. [127]. Copyright (2001) by the American Physical Society.

4. Concluding remarks

This review examines the influence of exchange interactions between transition-metal (TM) and rare-earth (RE) ions on absorption and luminescence phenomena. These interactions play a fundamental role in modulating optical properties, often giving rise to spectral features that differ significantly from those observed in isolated ions. As a result, spectroscopy serves as a powerful local probe for investigating magnetism, particularly in exchange-coupled systems and concentrated materials. By analyzing spectral features in relation to exchange interactions, valuable insights are gained into both local and long-range magnetic order, not only in the ground state but also in excited states. This establishes spectroscopy a unique tool for exploring excited-state magnetism and exciton dynamics in these materials.

The review focuses on TM/RE-doped halide and oxide materials, including concentrated systems. The role of exchange pathways is examined by studying materials of different dimensionality, featuring either well-defined sites or multiple sites capable of accommodating optically active ions. The results highlight the critical influence of TM/RE bonding in defining distinct superexchange pathways, each exerting unique influence on the energy-level scheme of the exchange-coupled system. Particular attention is given to Cr^{3+}, Mn^{2+}, Mn^{3+}, and Cu^{2+} systems, which exhibit spin-forbidden transitions activated by exchange interactions or highly distorted coordination environments due to the Jahn–Teller effect. These distortions create a rich electronic structure, allowing for establishing structural correlations and acting as non-radiative traps for excitons. In doubly or triply TM/RE-doped materials, exchange interactions play a crucial role in enabling new pathways for upconversion absorption or luminescence.

In conclusion, exchange interactions are pivotal in shaping the absorption and luminescence properties of materials. The findings highlight the impact of these interactions, suggesting that precise control over the host matrix or the application of external perturbations, such as pressure, can be strategically leveraged to engineer novel optical phenomena and enhance luminescence in concentrated materials.

CRediT authorship contribution statement

Diego Pérez-Francés: Writing – original draft, Resources, Investigation. **Fernando Rodríguez:** Writing – review & editing, Investigation, Funding acquisition. **Rafael Valiente:** Writing – review & editing, Supervision, Investigation, Funding acquisition, Conceptualization.

Declaration of competing interest

The authors declare that they have no known competing financial interests or personal relationships that could have appeared to influence the work reported in this paper.

Acknowledgments

This work was primarily supported by MICIU/AEI /10.13039/501100011033 and FEDER, UE through the projects PID2021-127656NB-I00 and PID2024-158839NB-I00. Additional support was received from University of Cantabria (project P254).

Data availability

No data was used for the research described in the article.

References

[1] A.L. Schawlow, D.L. Wood, A.M. Clogston, Electronic spectra of exchange-coupled ion pairs in crystals, Phys. Rev. Lett. 3 (6) (1959) 271–273, http://dx.doi.org/10.1103/PhysRevLett.3.271.

[2] D.S. McClure, Spectroscopy of magnetic insulators, in: B. Di Bartolo (Ed.), Optical Properties of Ions in Solids, Boston, MA, 1975, pp. 259–305, http://dx.doi.org/10.1007/978-1-4684-2787-5_9.

[3] Y. Tanabe, T. Moriya, S. Sugano, Magnon-induced electric dipole transition moment, Phys. Rev. Lett. 15 (26) (1965) 1023–1025, http://dx.doi.org/10.1103/PhysRevLett.15.1023.

[4] J. Ferguson, H. J. Guggenheim, Y. Tanabe, The effects of exchange interactions in the spectra of octahedral manganese. II. Compounds, J. Phys. Soc. Japan 21 (4) (1966) 692–704, http://dx.doi.org/10.1143/JPSJ.21.692.

[5] P.J. McCarthy, H.U. Güdel, Optical spectroscopy of exchange-coupled transition metal complexes, Coord. Chem. Rev. 88 (1988) 69–131, http://dx.doi.org/10.1016/0010-8545(88)80002-X.

[6] B. Henderson, G. Imbusch, Optical spectroscopy of inorganic solids, in: Monographs on the Physics and Chemistry of Materials, 2006.

[7] A.P. Vink, M.A. De Bruin, S. Roke, P.S. Peijzel, A. Meijerink, Luminescence of exchange coupled pairs of transition metal ions, J. Electrochem. Soc. 148 (7) (2001) E313, http://dx.doi.org/10.1149/1.1375169.

[8] K. Blazey, G. Burns, Cr^{3+}-Cr^{3+} ion exchange interactions in $LaAlO_3$, Phys. Lett. 15 (2) (1965) 117–119, http://dx.doi.org/10.1016/0031-9163(65)91298-9.

[9] J. Ferguson, H.J. Guggenheim, Y. Tanabe, Absorption of light by pairs of like and unlike transition-metal ions, Phys. Rev. Lett. 14 (18) (1965) 737–738, http://dx.doi.org/10.1103/PhysRevLett.14.737.

[10] J. Ferguson, H.J. Guggenheim, Y. Tanabe, Exchange effects in the electronic absorption spectrum of Mn(II) in perovskite fluorides, J. Appl. Phys. 36 (3) (1965) 1046–1047, http://dx.doi.org/10.1063/1.1714093.

[11] P. Kisliuk, W.F. Krupke, Exchange interactions between chromium ions in ruby, J. Appl. Phys. 36 (3) (1965) 1025–1026, http://dx.doi.org/10.1063/1.1714084.

[12] D.S. McClure, Optical spectra of exchange coupled Mn++ ion pairs in ZnS:MnS, J. Chem. Phys. 39 (11) (1963) 2850–2855, http://dx.doi.org/10.1063/1.1734115.

[13] J.P. Van Der Ziel, L.G. Van Uitert, Chromium-europium pair emission in $EuAlO_3$:Cr^{3+}, Phys. Rev. 180 (2) (1969) 343–349, http://dx.doi.org/10.1103/PhysRev.180.343.

[14] J. Vial, R. Buisson, Evidence for energy transfer induced by superexchange in LaF_3:Pr^{3+}, J. Physique Lett. 43 (21) (1982) 745–753, http://dx.doi.org/10.1051/jphyslet:019820043021074500.

[15] K.-I. Gondaira, Y. Tanabe, A note on the theory of superexchange interaction, J. Phys. Soc. Japan 21 (8) (1966) 1527–1548, http://dx.doi.org/10.1143/JPSJ.21.1527.

[16] S.M. Jacobsen, H.U. Guedel, W.E. Smith, Spin cluster excitations in Ti^{2+}-doped $MnCl_2$, Inorg. Chem. 26 (12) (1987) 2001–2005, http://dx.doi.org/10.1021/ic00259a038.

[17] P.J. McCarthy, H.U. Güdel, Optical spectra of exchange-coupled manganese(II) pairs in cesium magnesium trichloride and cesium magnesium tribromide, Inorg. Chem. 23 (7) (1984) 880–887, http://dx.doi.org/10.1021/ic00175a018.

[18] H.U. Güdel, Singly and doubly excited states of exchange-coupled dimers, Comments Inorg. Chem. 3 (4) (1984) 189–204, http://dx.doi.org/10.1080/02603598408078137.

[19] H.U. Güdel, L. Dubicki, The electronic spectrum of μ-oxo-bis[pentammine chromium(III)] ion, Chem. Phys. 6 (2) (1974) 272–281, http://dx.doi.org/10.1016/0301-0104(74)85067-6.

[20] G.L. McPherson, T.J. Kistenmacher, J.B. Folkers, G.D. Stucky, Effect of exchange coupling on the spectra of transition metal ions. The ligand field spectrum and crystal structure of $CsCrCl_3$, J. Chem. Phys. 57 (9) (1972) 3771–3780, http://dx.doi.org/10.1063/1.1678843.

[21] H. Riesen, H.U. Güdel, Exchange interactions in a trigonal chromium(III) pair: Optical spectroscopy of tris-(μ-hydroxo)-bis-[(1,4,7-trimethyl-1,4,7-triazacyclononane) chromium(III)] triperchlorate, Mol. Phys. 60 (6) (1987) 1221–1244, http://dx.doi.org/10.1080/00268978700100811.

[22] O.S. Wenger, D.R. Gamelin, H.U. Güdel, Chemical modification of transition metal upconversion properties: Exchange enhancement of Ni^{2+} upconversion rates in Ni^{2+}:$RbMnCl_3$, J. Am. Chem. Soc. 122 (30) (2000) 7408–7409, http://dx.doi.org/10.1021/ja000979o.

[23] P. Gerner, C. Reinhard, H.U. Güdel, Cooperative near-IR to visible photon upconversion in Yb^{3+}-doped $MnCl_2$ and $MnBr_2$: Comparison with a series of Yb^{3+}-doped Mn^{2+} halides, Chem. – Eur. J. 10 (19) (2004) 4735–4741, http://dx.doi.org/10.1002/chem.200400282.

[24] H. Weihe, H.U. Güdel, Quantitative interpretation of the goodenough-kanamori rules: A critical analysis, Inorg. Chem. 36 (17) (1997) 3632–3639, http://dx.doi.org/10.1021/ic961502+.

[25] P.W. Anderson, New approach to the theory of superexchange interactions, Phys. Rev. 115 (1) (1959) 2–13, http://dx.doi.org/10.1103/PhysRev.115.2.

[26] J. Goodenough, Magnetism and the chemical bond, in: Inorganic Chemistry Section / Interscience Monographs on Chemistry, 1963.

[27] P.J. Hay, J.C. Thibeault, R. Hoffmann, Orbital interactions in metal dimer complexes, J. Am. Chem. Soc. 97 (17) (1975) 4884–4899, http://dx.doi.org/10.1021/ja00850a018.

[28] J. Hubbard, Electron correlations in narrow energy bands, Proc. R. Soc. Lond. Ser. A. Math. Phys. Sci. 276 (1365) (1963) 238–257, http://dx.doi.org/10.1098/rspa.1963.0204.

[29] H.B. Gray, C. Ballhausen, A molecular orbital theory for square planar metal complexes, J. Am. Chem. Soc. 85 (3) (1963) 260–265, http://dx.doi.org/10.1021/ja00886a002.

[30] R. Orbach, Relaxation and energy transfer, in: B. Di Bartolo (Ed.), Optical Properties of Ions in Solids, Boston, MA, 1975, pp. 355–399, http://dx.doi.org/10.1007/978-1-4684-2787-5_12.

[31] P.A.M. Dirac, On the theory of quantum mechanics, Proc. R. Soc. Lond. Ser. A, Contain. Pap. A Math. Phys. Character 112 (762) (1926) 661–677, http://dx.doi.org/10.1098/rspa.1926.0133.

[32] W. Heisenberg, Zur theorie des ferromagnetismus, Z. Phys. 49 (9) (1928) 619–636, http://dx.doi.org/10.1007/BF01328601.

[33] J. Van Vleck, The dirac vector model in complex spectra, Phys. Rev. 45 (6) (1934) 405, http://dx.doi.org/10.1103/PhysRev.45.405.

[34] P.W. Anderson, Antiferromagnetism. theory of superexchange interaction, Phys. Rev. 79 (2) (1950) 350–356, http://dx.doi.org/10.1103/PhysRev.79.350.

[35] J.H. Van Vleck, On the theory of antiferromagnetism, J. Chem. Phys. 9 (1) (1941) 85–90, http://dx.doi.org/10.1063/1.1750830.

[36] L.J. De Jongh, Experiments on simple magnetic model systems, J. Appl. Phys. 49 (3) (1978) 1305–1310, http://dx.doi.org/10.1063/1.325027.

[37] B. Bleaney, K.D. Bowers, Anomalous paramagnetism of copper acetate, Proc. R. Soc. Lond. Ser. A. Math. Phys. Sci. 214 (1119) (1952) 451–465, http://dx.doi.org/10.1098/rspa.1952.0181.

[38] H. Riesen, H.U. Güdel, Excitation energy transfer between inequivalent chromium(III) dimers in $[(NH_3)_5CrOHCr(NH_3)_5]Cl_5{\cdot}H_2O$, Mol. Phys. 58 (3) (1986) 509–534, http://dx.doi.org/10.1080/00268978600101331.

[39] D.S. Rodbell, I.S. Jacobs, J. Owen, E.A. Harris, Biquadratic exchange and the behavior of some antiferromagnetic substances, Phys. Rev. Lett. 11 (1) (1963) 10, http://dx.doi.org/10.1103/PhysRevLett.11.10.

[40] Y. Tanabe, S. Sugano, On the absorption spectra of complex ions II, J. Phys. Soc. Japan 9 (5) (1954) 766–779, http://dx.doi.org/10.1143/JPSJ.9.766.

[41] M. Naito, Cr^{3+} ion pair spectrum in ruby, J. Phys. Soc. Japan 34 (6) (1973) 1491–1502, http://dx.doi.org/10.1143/JPSJ.34.1491.

[42] C. Ronda, T. Amrein, Evidence for exchange-induced luminescence in Zn_2SiO_4:Mn, J. Lumin. 69 (5–6) (1996) 245–248, http://dx.doi.org/10.1016/S0022-2313(96)00103-2.

[43] M. Atanasov, C. Daul, H.U. Güdel, Modelling of anisotropic exchange coupling in rare-earth–transition-metal pairs: Applications to Yb^{3+}-Mn^{2+} and Yb^{3+}-Cr^{3+} halide clusters and implications to the light up-conversion, in: Computational Chemistry: Reviews of Current Trends, vol. 9, 2005, pp. 153–194, http://dx.doi.org/10.1142/9789812701305_0005.

[44] U. Lanver, G. Lehmann, Luminescence spectra of Mn(II) in different symmetries, J. Lumin. 17 (2) (1978) 225–235, http://dx.doi.org/10.1016/0022-2313(78)90088-1.

[45] A. Stevels, Red Mn^{2+}-luminescence in hexagonal aluminates, J. Lumin. 20 (2) (1979) 99–109, http://dx.doi.org/10.1016/0022-2313(79)90041-3.

[46] H. Siebold, J. Heber, Energy transfer in $LaAlO_3$:Cr^{3+}, J. Lumin. 23 (3–4) (1981) 325–347, http://dx.doi.org/10.1016/0022-2313(81)90138-1.

[47] J. Derkosch, W. Mikenda, A. Preisinger, N-lines and chromium-pairs in the luminescence spectra of the spinels $ZnAl_2O_4$:Cr^{3+} and $MgAl_2O_4$:Cr^{3+}, J. Solid State Chem. 22 (2) (1977) 127–133, http://dx.doi.org/10.1016/0022-4596(77)90029-9.

[48] C. Ronda, Phosphors for lamps and displays: an applicational view, J. Alloys Compd. 225 (1–2) (1995) 534–538, http://dx.doi.org/10.1016/0925-8388(94)07065-2.

[49] W. Busse, H.-E. Gumlich, B. Meissner, D. Theis, Time resolved spectroscopy of ZnS:Mn by dye laser technique, J. Lumin. 12–13 (1976) 693–700, http://dx.doi.org/10.1016/0022-2313(76)90163-0.

[50] L.R. Bradshaw, J.W. May, J.L. Dempsey, X. Li, D.R. Gamelin, Ferromagnetic excited-state Mn^{2+} dimers in $Zn_{1-x}Mn_xSe$ quantum dots observed by time-resolved magnetophotoluminescence, Phys. Rev. B 89 (11) (2014) 115312, http://dx.doi.org/10.1103/PhysRevB.89.115312.

[51] C. Barthou, J. Benoit, P. Benalloul, A. Morell, Mn^{2+} concentration effect on the optical properties of Zn_2SiO_4:Mn phosphors, J. Electrochem. Soc. 141 (2) (1994) 524–528, http://dx.doi.org/10.1149/1.2054759.

[52] A. Stevels, A. Vink, Fine structure in the low temperature luminescence of Zn_2SiO_4:Mn and $Mg_4Ta_2O_9$:Mn, J. Lumin. 8 (6) (1974) 443–451, http://dx.doi.org/10.1016/0022-2313(74)90009-X.

[53] Z.T. Chen, E.H. Song, M. Wu, B. Zhou, Q.Y. Zhang, Exchange coupled Mn-Mn pair: An approach for super-broadband 1380 nm emission in α-MnS, Appl. Phys. Lett. 109 (19) (2016) 191907, http://dx.doi.org/10.1063/1.4967452.

[54] E. Song, S. Ding, M. Wu, S. Ye, F. Xiao, S. Zhou, Q. Zhang, Anomalous NIR luminescence in Mn^{2+}-doped fluoride perovskite nanocrystals, Adv. Opt. Mater. 2 (7) (2014) 670–678, http://dx.doi.org/10.1002/adom.201400066.

[55] E.H. Song, J.L. Wang, D.C. Yu, S. Ye, Q.Y. Zhang, Anomalous tunable visible to near infrared emission in the Mn^{2+}-doped spinel $MgGa_2O_4$ and room-temperature upconversion in the Mn^{2+} and Yb^{3+}-codoped spinel, J. Mater. Chem. C 2 (41) (2014) 8811–8816, http://dx.doi.org/10.1039/C4TC01681E.

[56] E. Song, J. Wang, S. Ye, X.-B. Yang, M. Peng, Q. Zhang, L. Wondraczek, Wavelength-tunability and multiband emission from single-site Mn^{2+} doped CaO through antiferromagnetic coupling and tailored superexchange reactions, Adv. Opt. Mater. 5 (13) (2017) 1700070, http://dx.doi.org/10.1002/adom.201700070.

[57] A.J. Van Bunningen, S.T. Keizer, A. Meijerink, Understanding enormous red-shifts in highly concentrated Mn^{2+} phosphors, J. Mater. Chem. C 11 (26) (2023) 8961–8970, http://dx.doi.org/10.1039/D3TC00778B.

[58] D.J. Robbins, E.E. Mendez, E.A. Giess, I.F. Chang, Pairing effects in the luminescence spectrum of Zn_2SiO_4:Mn, J. Electrochem. Soc. 131 (1) (1984) 141–146, http://dx.doi.org/10.1149/1.2115496.

[59] N. Yamashita, S. Maekawa, K. Nakamura, Influence of paired Mn^{2+} centers on the luminescence spectra of CaS:Mn^{2+}, Japan. J. Appl. Phys. 29 (9R) (1990) 1729, http://dx.doi.org/10.1143/JJAP.29.1729.

[60] W.H. Brumage, C.R. Yarger, C.C. Lin, Effect of the exchange coupling of Mn++ ions on the magnetic susceptibilities of Zns:MnS crystals, Phys. Rev. 133 (3A) (1964) A765, http://dx.doi.org/10.1103/PhysRev.133.A765.

[61] S.T. Ochsenbein, Y. Feng, K.M. Whitaker, E. Badaeva, W.K. Liu, X. Li, D.R. Gamelin, Charge-controlled magnetism in colloidal doped semiconductor nanocrystals, Nature Nanotechnology 4 (10) (2009) 681–687, http://dx.doi.org/10.1038/nnano.2009.221.

[62] R. Viswanatha, J.M. Pietryga, V.I. Klimov, S.A. Crooker, Spin-polarized Mn^{2+} emission from mn-doped colloidal nanocrystals, Phys. Rev. Lett. 107 (6) (2011) 067402, http://dx.doi.org/10.1103/PhysRevLett.107.067402.

[63] D. Langer, S. Ibuki, Zero-phonon lines and phonon coupling in ZnS:Mn, Phys. Rev. 138 (3A) (1965) A809–A815, http://dx.doi.org/10.1103/PhysRev.138.A809.

[64] D. Fournier, A. Boccara, J. Rivoal, Magneto-optical study of $^4T_1$ state of Mn^{2+} in ZnS, J. Phys. C: Solid State Phys. 10 (1) (1977) 113, http://dx.doi.org/10.1088/0022-3719/10/1/017.

[65] B. Morosin, E.J. Graber, Crystal structure of tetramethylammonium manganese(II) chloride, Acta Crystallogr. 23 (5) (1967) 766–770, http://dx.doi.org/10.1107/S0365110X67003688.

[66] S. Tancharakorn, F.P.A. Fabbiani, D.R. Allan, K.V. Kamenev, N. Robertson, Combined magnetic and single-crystal X-ray structural study of the linear chain antiferromagnet $[(CH_3)_4N][MnCl_3]$ under varying pressure, J. Am. Chem. Soc. 128 (28) (2006) 9205–9210, http://dx.doi.org/10.1021/ja061923i.

[67] R.A. Auerbach, G.L. McPherson, Emission dynamics from doped crystals of $(CH_3)_4NMnCl_3$ (TMMC): Exciton trapping in a one-dimensional lattice, Phys. Rev. B 33 (10) (1986) 6815–6820, http://dx.doi.org/10.1103/PhysRevB.33.6815.

[68] M.F. Herman, W.J. Rodriguez, G.L. McPherson, One-dimensional exciton migration: The role of trap efficiency, Chem. Phys. Lett. 144 (5–6) (1988) 541–547, http://dx.doi.org/10.1016/0009-2614(88)87311-1.

[69] R. Knochenmuss, H.U. Güdel, Exciton trapping in the one-dimensional antiferromagnet $[(CH_3)_4N]MnCl_3$, J. Chem. Phys. 86 (3) (1987) 1104–1110, http://dx.doi.org/10.1063/1.452251.

[70] R. Kroon, H. Fleurent, R. Sprik, Diffusion-limited exciton fusion reaction in one-dimensional tetramethylammonium manganese trichloride (TMMC), Phys. Rev. E 47 (4) (1993) 2462–2472, http://dx.doi.org/10.1103/PhysRevE.47.2462.

[71] L. Nataf, F. Rodríguez, R. Valiente, J. González, Spectroscopic and luminescence properties of $(CH_3)_4NMnCl_3$: A sensitive Mn^{2+}-based pressure gauge, High Press. Res. 29 (4) (2009) 653–659, http://dx.doi.org/10.1080/08957950903414979.

[72] L. Nataf, J.A. Barreda-Argüeso, R. Valiente, J. González, F. Rodríguez, Effects of Cu^{2+} doping and pressure on the exchange-mediated exciton dynamics in one-dimensional $N(CH_3)_4MnCl_3$, Phys. Rev. B 89 (11) (2014) 115120, http://dx.doi.org/10.1103/PhysRevB.89.115120.

[73] F. Rodríguez, I. Hernández, M. Moreno, R. Alcalá, Photoluminescence and radiationless processes in Mn^{2+}-doped $Ca_{1-x}Sr_xF_2$ fluorites as a function of pressure and temperature: A structural correlation study, J. Chem. Phys. 119 (16) (2003) 8686–8694, http://dx.doi.org/10.1063/1.1611874.

[74] M.T. Candela, E. Jara, F. Aguado, R. Valiente, F. Rodríguez, Structural correlations in Jahn–Teller systems of Mn^{3+} and cu^{2+}: Unraveling local structures through spectroscopic techniques, J. Phys. Chem. C 124 (41) (2020) 22692–22703, http://dx.doi.org/10.1021/acs.jpcc.0c07243.

[75] P. Köhler, W. Massa, D. Reinen, B. Hofmann, R. Hoppe, Der Jahn-Teller-Effekt des Mn^{3+} -Ions in oktaedrischer Fluorkoordination. Ligandenfeldspektroskopische und magnetische Untersuchungen, Z. Anorg. Allg. Chem. 446 (1) (1978) 131–158, http://dx.doi.org/10.1002/zaac.19784460114.

[76] W. Massa, Structural chemistry and Jahn-Teller effect in fluoromanganates(III), Rev. Inorg. Chem. 19 (1–2) (1999) 117–183, http://dx.doi.org/10.1515/REVIC.1999.19.1-2.117.

[77] W. Massa, D. Babel, Crystal structure and bonding in transition-metal fluoro compounds, Chem. Rev. 88 (1) (1988) 275–296, http://dx.doi.org/10.1021/cr00083a013.

[78] F. Palacio, M.C. Morón, Magneto-structural correlations in Mn(III) fluorides, in: Research Frontiers in Magnetochemistry, 1993, pp. 227–281, http://dx.doi.org/10.1142/9789814354615_0009.

[79] F. Rodríguez, P. Nuñez, M. Marco De Lucas, Polarized optical absorption spectroscopy of the $Tl_2MnF_5{\cdot}H_2O$ 1D manganese (III) single crystal, J. Solid State Chem. 110 (2) (1994) 370–383, http://dx.doi.org/10.1006/jssc.1994.1182.

[80] F. Rodríguez, F. Aguado, Correlations between structure and optical properties in Jahn–Teller Mn^{3+} fluorides: A study of $TlMnF_4$ and $NaMnF_4$ under pressure, J. Chem. Phys. 118 (24) (2003) 10867–10875, http://dx.doi.org/10.1063/1.1569847.

[81] A. Tressaud, J.-M. Dance, Relationships between structure and low-dimensional magnetism in fluorides, in: M.J. Clarke, J.B. Goodenough, J.A. Ibers, C. Klixbüll Jørgensen, J.B. Neilands, D. Reinen, R. Weiss, R.J.P. Williams (Eds.), in: Structures Versus Special Properties, vol. 52, Berlin, Heidelberg, 1982, pp. 87–146, http://dx.doi.org/10.1007/BFb0111297, Series Title: Structure and Bonding.

[82] W. Massa, Struktur von natrium-pentafluoromanganat(III), Acta Crystallogr. Sect. C Cryst. Struct. Commun. 42 (6) (1986) 644–647, http://dx.doi.org/10.1107/S0108270186095069.

[83] M. Molinier, W. Massa, S. Khairoun, A. Tressaud, J.L. Soubeyroux, Crystal and magnetic structures of $NaMnF_4$, Z. Naturforschung B 46 (12) (1991) 1669–1673, http://dx.doi.org/10.1515/znb-1991-1214.

[84] J.M. De Teresa, M.R. Ibarra, J. Blasco, J. García, C. Marquina, P.A. Algarabel, Z. Arnold, K. Kamenev, C. Ritter, R. Von Helmolt, Spontaneous behavior and magnetic field and pressure effects on $La_{2/3}Ca_{1/3}MnO_3$ perovskite, Phys. Rev. B 54 (2) (1996) 1187–1193, http://dx.doi.org/10.1103/PhysRevB.54.1187.

[85] J. Blasco, J. García, J.M. De Teresa, M.R. Ibarra, J. Perez, P.A. Algarabel, C. Marquina, C. Ritter, Structural, magnetic, and transport properties of the giant magnetoresistive perovskites $La_{2/3}Ca_{1/3}Mn_{1-x}Al_xO_{3-\delta}$, Phys. Rev. B 55 (14) (1997) 8905–8910, http://dx.doi.org/10.1103/PhysRevB.55.8905.

[86] F. Aguado, F. Rodriguez, P. Núñez, Pressure-induced Jahn-Teller suppression and simultaneous high-spin to low-spin transition in the layered perovskite $CsMnF_4$, Phys. Rev. B 76 (9) (2007) 094417, http://dx.doi.org/10.1103/PhysRevB.76.094417.

[87] M.C. Morón, F. Palacio, S.M. Clark, A. Paduan-Filho, Structural and magnetic behavior of the s=2 layered ferromagnet $CsMnF_4$ under hydrostatic pressure, Phys. Rev. B 51 (13) (1995) 8660–8663, http://dx.doi.org/10.1103/PhysRevB.51.8660.

[88] M.C. Morón, F. Palacio, S.M. Clark, Pressure-induced structural phase transitions in the $AMnF_4$ series (A=Cs, Rb, K) studied by synchrotron X-ray powder diffraction: Correlation between hydrostatic and chemical pressure, Phys. Rev. B 54 (10) (1996) 7052–7061, http://dx.doi.org/10.1103/PhysRevB.54.7052.

[89] F. Rodríguez, F. Aguado, J.-P. Itié, M. Hanfland, Structural correlation in Jahn–Teller systems of Cu^{2+} and Mn^{3+} under pressure, J. Phys. Soc. Japan 76 (Suppl.A) (2007) 1–4, http://dx.doi.org/10.1143/JPSJS.76SA.1.

[90] R. Valiente, O. Wenger, H.U. Güdel, New photon upconversion processes in Yb^{3+} doped csmncl$_3$ and rbmncl$_3$, Chem. Phys. Lett. 320 (5–6) (2000) 639–644, http://dx.doi.org/10.1016/S0009-2614(00)00278-5.

[91] F. Auzel, Compteur quantique par transfert d'energie entre deux ions de terres rares dans un tungstate mixte et dans un verre, CR Acad. Sci. Paris 262 (1966) 1016–1019.

[92] S. Heer, K. Kömpe, H.-U. Güdel, M. Haase, Highly efficient multicolour upconversion emission in transparent colloids of lanthanide-doped $NaYF_4$ nanocrystals, Adv. Mater. 16 (23–24) (2004) 2102–2105, http://dx.doi.org/10.1002/adma.200400772.

[93] E. Heumann, S. Bär, K. Rademaker, G. Huber, S. Butterworth, A. Diening, W. Seelert, Semiconductor-laser-pumped high-power upconversion laser, Appl. Phys. Lett. 88 (6) (2006) http://dx.doi.org/10.1063/1.2172293.

[94] M. Nyk, R. Kumar, T.Y. Ohulchanskyy, E.J. Bergey, P.N. Prasad, High contrast in vitro and in vivo photoluminescence bioimaging using near infrared to near infrared up-conversion in Tm^{3+} and Yb^{3+} doped fluoride nanophosphors, Nano Lett. 8 (11) (2008) 3834–3838, http://dx.doi.org/10.1021/nl802223f.

[95] T. Trupke, A. Shalav, B. Richards, P. Würfel, M. Green, Efficiency enhancement of solar cells by luminescent up-conversion of sunlight, Sol. Energy Mater. Sol. Cells 90 (18–19) (2006) 3327–3338, http://dx.doi.org/10.1016/j.solmat.2005.09.021.

[96] R. Valiente, O.S. Wenger, H.U. Güdel, Near-infrared-to-visible photon upconversion process induced by exchange interactions in Yb^{3+}-doped $RbMnCl_3$, Phys. Rev. B 63 (16) (2001) 165102, http://dx.doi.org/10.1103/PhysRevB.63.165102.

[97] Z.J. Kiss, R.C. Duncan, Cross-pumped Cr^{3+}-Nd^{3+}:YAG laser system, Appl. Phys. Lett. 5 (10) (1964) 200–202, http://dx.doi.org/10.1063/1.1723587.

[98] V. Ovsyankin, P. Feofilov, Mechanism of summation of electronic excitations in activated crystals, Sov. J. Exp. Theor. Phys. Lett. 3 (1966) 322.

[99] M. Altarelli, D. Dexter, Cooperative energy transfer and photon absorption, Opt. Commun. 2 (1) (1970) 36–38, http://dx.doi.org/10.1016/0030-4018(70)90025-8.

[100] F. Ostermayer, Jr., J. Van Der Ziel, H. Marcos, L. Van Uitert, J. Geusic, Frequency upconversion in YF_3:Yb^{3+},Tm^{3+}, Phys. Rev. B 3 (8) (1971) 2698, http://dx.doi.org/10.1103/PhysRevB.3.2698.

[101] R. Watts, H. Richter, Diffusion and transfer of optical excitation in YF_3:Yb,ho, Phys. Rev. B 6 (4) (1972) 1584, http://dx.doi.org/10.1103/PhysRevB.6.1584.

[102] R. Valiente, O.S. Wenger, H.U. Güdel, Upconversion luminescence in Yb^{3+} doped $CsMnCl_3$: Spectroscopy, dynamics, and mechanisms, J. Chem. Phys. 116 (12) (2002) 5196–5204, http://dx.doi.org/10.1063/1.1446430.

[103] C. Reinhard, R. Valiente, H.U. Güdel, Exchange-induced upconversion in Rb_2MnCl_4:Yb^{3+}, J. Phys. Chem. B 106 (39) (2002) 10051–10057, http://dx.doi.org/10.1021/jp0203797.

[104] P. Gerner, O.S. Wenger, R. Valiente, H.U. Güdel, Green and red light emission by upconversion from the near-IR in Yb^{3+} doped $CsMnBr_3$, Inorg. Chem. 40 (18) (2001) 4534–4542, http://dx.doi.org/10.1021/ic010081f.

[105] R. Martín-Rodríguez, R. Valiente, F. Rodríguez, F. Piccinelli, A. Speghini, M. Bettinelli, Temperature dependence and temporal dynamics of Mn^{2+} upconversion luminescence sensitized by Yb^{3+} in codoped $LaMgAl_{11}O_{19}$, Phys. Rev. B 82 (7) (2010) 075117, http://dx.doi.org/10.1103/PhysRevB.82.075117.

[106] E. Ejder, Methods of representing emission, excitation, and photoconductivity spectra, J. Opt. Soc. Am. 59 (2) (1969) 223–224, http://dx.doi.org/10.1364/JOSA.59.0223_1.

[107] D.R. Gamelin, H.U. Güdel, Upconversion processes in transition metal and rare earth metal systems, in: A. De Meijere, H. Kessler, S.V. Ley, J. Thiem, F. Vögtle, K.N. Houk, J.-M. Lehn, S.L. Schreiber, B.M. Trost, H. Yamamoto, H. Yersin (Eds.), in: Transition Metal and Rare Earth Compounds, vol. 214, Berlin, Heidelberg, 2001, pp. 1–56, http://dx.doi.org/10.1007/3-540-44474-2_1, Series Title: Topics in Current Chemistry.

[108] P. Gerner, C. Fuhrer, C. Reinhard, H.U. Güdel, Near-infrared to visible photon upconversion in Mn^{2+} and Yb^{3+} containing materials, J. Alloys Compd. 380 (1–2) (2004) 39–44, http://dx.doi.org/10.1016/j.jallcom.2004.03.017.

[109] C. Reinhard, P. Gerner, F. Rodriguez, S. Garcia-Revilla, R. Valiente, H.U. Güdel, Near-infrared to green photon upconversion in Mn^{2+} and Yb^{3+} doped lattices, Chem. Phys. Lett. 386 (1–3) (2004) 132–136, http://dx.doi.org/10.1016/j.cplett.2003.12.127.

[110] R. Martín-Rodríguez, R. Valiente, M. Bettinelli, Room-temperature green upconversion luminescence in $LaMgAl_{11}O_{19}$:Mn^{2+},Yb^{3+} upon infrared excitation, Appl. Phys. Lett. 95 (9) (2009) 091913, http://dx.doi.org/10.1063/1.3220059.

[111] J. Ferguson, H.J. Guggenheim, E.R. Krausz, Optical absorption by Cu-Mn pairs in $KZnF_3$, J. Phys. C: Solid State Phys. 4 (13) (1971) 1866–1873, http://dx.doi.org/10.1088/0022-3719/4/13/037.

[112] J. Ferguson, H.J. Guggenheim, Electron-transfer states of pairs of unlike transition-metal ions in perovskite fluorides, Phys. Rev. B 1 (11) (1970) 4223–4228, http://dx.doi.org/10.1103/PhysRevB.1.4223.

[113] C. Mathoniere, O. Kahn, Optical properties of and spin interaction in the trinuclear compound $\{[Mn(Me_6\text{-}[14]ane\text{-}N_4)]_2Cu(pba)\}(CF_3SO_3)_2{\cdot}2H_2O$, Inorg. Chem. 33 (10) (1994) 2103–2108, http://dx.doi.org/10.1021/ic00088a009.

[114] C. Mathoniere, O. Kahn, J.C. Daran, H. Hilbig, F.H. Koehler, Complementarity and internal consistency between magnetic and optical properties for the $Mn^{II}cu^{II}$ heterodinuclear compound $[Mn(Me_6\text{-}[14]ane\text{-}N_4)Cu(oxpn)](CF_3SO_3)_2$ (Me_6-[14]ane-N_4= (±)-5,7,7,12,14,14-Hexamethyl-1,4,8,11-tetraazacyclotetradecane; oxpn=N,N'-Bis(3-aminopropyl)oxamide), Inorg. Chem. 32 (19) (1993) 4057–4062, http://dx.doi.org/10.1021/ic00071a015.

[115] O. Cador, C. Mathonière, O. Kahn, Optical absorption spectroscopy of the tetranuclear compound $[Mn\{Cu(oxpn)\}_3](ClO_4)_2{\cdot}2H_2O$ (oxpn=N,N'-Bis(3-aminopropyl)oxamide): Complementarity with magnetic properties, Inorg. Chem. 36 (9) (1997) 1923–1928, http://dx.doi.org/10.1021/ic960857q.

[116] O. Cador, C. Mathonière, O. Kahn, J.-P. Costes, M. Verelst, P. Lecante, Spectroscopic determination of magnetic exchange parameters and structural geometry for trinuclear compounds: $(CuL)_2Mn{\cdot}xB$ (L= N-(4-Methyl-6-oxo-3-azahept-4-enyl)oxamato and B= $(CH_3)_2SO$ (x=2) or H_2O (x =5)), Inorg. Chem. 38 (11) (1999) 2643–2648, http://dx.doi.org/10.1021/ic981147i.

[117] J. Ferré, M. Régis, Optical determination of the Cu-Mn - exchange interaction in $K_2Cu_{1-x}Mn_xF_4$, Solid State Commun. 26 (4) (1978) 225–228, http://dx.doi.org/10.1016/0038-1098(78)90259-4.

[118] C. Windsor, R. Stevenson, Spin waves in $RbMnF_3$, Proc. Phys. Soc. 87 (2) (1966) 501, http://dx.doi.org/10.1088/0370-1328/87/2/319.

[119] I. Yamada, Magnetic properties of K_2CuF_4 -A transparent two-dimensional ferromagnet-, J. Phys. Soc. Japan 33 (4) (1972) 979–988, http://dx.doi.org/10.1143/JPSJ.33.979.

[120] R. Valiente, F. Rodríguez, Polarized electronic spectra of the $(CH_3NH_3)_2Cd_{1-x}Mn_xCl_4$ (x=0-1) perovskite layer doped with Cu^{2+}: Study of the $Cl^- \rightarrow Cu^{2+}$ charge transfer intensity enhancement along the series, J. Phys. Chem. Solids 57 (5) (1996) 571–587, http://dx.doi.org/10.1016/0022-3697(96)00293-4.

[121] R.D. Willett, D. Gatteschi, O. Kahn, Magneto-Structural Correlations in Exchange Coupled Systems, Technical Report, D. Reidel Publishing Co., Hingham, MA, 1985.

[122] J. Ferguson, H.J. Guggenheim, Y. Tanabe, Simultaneous electronic excitation of exchange-coupled pairs of manganese and nickel ions, Phys. Rev. 161 (2) (1967) 207–212, http://dx.doi.org/10.1103/PhysRev.161.207.

[123] J. Ferguson, H.J. Guggenheim, Y. Tanabe, Absorption of light by pairs of exchange-coupled manganese and nickel ions in cubic perovskite fluorides, J. Chem. Phys. 45 (4) (1966) 1134–1141, http://dx.doi.org/10.1063/1.1727728.

[124] M. Kasha, Characterization of electronic transitions in complex molecules, Discuss. Faraday Soc. 9 (1950) 14, http://dx.doi.org/10.1039/df9500900014.

[125] R. Moncorgé, T. Benyattou, Excited-state absorption of Ni^{2+} in MgF_2 and MgO, Phys. Rev. B 37 (16) (1988) 9186–9196, http://dx.doi.org/10.1103/PhysRevB.37.9186.

[126] U. Oetliker, M. Riley, P. May, H. Güdel, Excited state dynamics in Ni^{2+}-doped $CsCdCl_3$: Excitation avalanche, Coord. Chem. Rev. 111 (1991) 125–130, http://dx.doi.org/10.1016/0010-8545(91)84017-Y.

[127] O.S. Wenger, R. Valiente, H.U. Güdel, Optical spectroscopy of the Ni^{2+}-doped layer perovskites Rb_2MCl_4 (M=Cd, Mn): Effects of Ni^{2+}-Mn^{2+} exchange interactions on the Ni^{2+} absorption, luminescence, and upconversion properties, Phys. Rev. B 64 (23) (2001) 235116, http://dx.doi.org/10.1103/PhysRevB.64.235116.

[128] L.L. Lohr, D.S. McClure, Optical spectra of divalent manganese salts. II. The effect of interionic coupling on absorption strength, J. Chem. Phys. 49 (8) (1968) 3516–3521, http://dx.doi.org/10.1063/1.1670626.

[129] O.S. Wenger, H.U. Güdel, Photon upconversion properties of Ni^{2+} in magnetic and nonmagnetic chloride host lattices, Inorg. Chem. 40 (1) (2001) 157–164, http://dx.doi.org/10.1021/ic000662p.

[130] J. Goodyear, E.M. Ali, G.A. Steigmann, Rubidium tetrachloromanganate, Acta Crystallogr. Sect. B Struct. Crystallogr. Cryst. Chem. 33 (9) (1977) 2932–2933, http://dx.doi.org/10.1107/S0567740877009868.

[131] H.J. Seifert, F.W. Koknat, Neue Alkalichlorocadmate(II) in den Systemen $CsCl/CdCl_2$ und $RbCl/CdCl_2$, Z. Anorg. Allg. Chem. 357 (4–6) (1968) 314–324, http://dx.doi.org/10.1002/zaac.19683570419.

[132] H.U. Güdel, Magnetic and optical excitations in clusters, in: D. Gatteschi, O. Kahn, J.S. Miller, F. Palacio (Eds.), Magnetic Molecular Materials, Dordrecht, 1991, pp. 333–352, http://dx.doi.org/10.1007/978-94-011-3254-1_23.

[133] H. Hoekstra, C. Ronda, C. Haas, Giant-spin clusters in MnI_2:Ni, Physica B+C 122 (3) (1983) 295–301, http://dx.doi.org/10.1016/0378-4363(83)90056-6.

[134] J. Kanamori, Superexchange interaction and symmetry properties of electron orbitals, J. Phys. Chem. Solids 10 (2–3) (1959) 87–98, http://dx.doi.org/10.1016/0022-3697(59)90061-7.

[135] J. Goodyear, G.A. Steigmann, E.M. Ali, Rubidium trichloromanganate, Acta Crystallogr. Sect. B Struct. Crystallogr. Cryst. Chem. 33 (1) (1977) 256–258, http://dx.doi.org/10.1107/S0567740877003264.